


Evolutionary and immune microenvironment dynamics during neoadjuvant treatment of esophageal adenocarcinoma

Received: 26 March 2023

Accepted: 21 March 2025

Published online: 14 May 2025

 Check for updates

Melissa Barroux ^{1,2,3}✉, Jacob Househam^{1,4}, Eszter Lakatos ^{1,5}, Tahel Ronel ^{1,5,6}, Ann-Marie Baker ^{1,5}, Henrike Salié ⁷, Maximilian Mossner^{1,5}, Kane Smith^{1,5}, Chris Kimberley¹, Salpie Nowinski^{1,5}, Alison Berner¹, Vinaya Gunasri^{1,8}, Martin Borgmann ⁷, Sven Liffers^{9,10}, Marnix Jansen ⁸, Giulio Caravagna ¹¹, Katja Steiger ¹², Julia Slotta-Huspenina^{13,14}, Wilko Weichert¹³, Luis Zapata⁵, Eleftheria Gioti⁵, Sylvie Lorenzen¹⁵, Markus Alberstmeier¹⁶, Benny Chain ⁶, Helmut Friess¹⁷, Bertram Bengsch ^{7,18,19}, Roland M. Schmid^{2,3}, Jens T. Siveke ^{9,10}, Michael Quante ^{2,7,19,20} & Trevor A. Graham ^{1,5,20}✉

Locally advanced esophageal adenocarcinoma remains difficult to treat and the ecological and evolutionary dynamics responsible for resistance and recurrence are incompletely understood. Here, we performed longitudinal multiomic analysis of patients with esophageal adenocarcinoma in the MEMORI trial. Multi-region multi-timepoint whole-exome and paired transcriptome sequencing was performed on 27 patients before, during and after neoadjuvant treatment. We found major transcriptomic changes during treatment with upregulation of immune, stromal and oncogenic pathways. Genetic data revealed that clonal sweeps through treatment were rare. Imaging mass cytometry and T cell receptor sequencing revealed remodeling of the tumor microenvironment during treatment. The presence of genetic immune escape, a less-cytotoxic T cell phenotype and a lack of clonal T cell expansions were linked to poor treatment response. In summary, there were widespread transcriptional and environmental changes through treatment, with limited clonal replacement, suggestive of phenotypic plasticity.

Esophageal cancer is the sixth most common cause of cancer-related death worldwide, with a median overall survival of <1 year¹. Incidence rates for esophageal adenocarcinoma (EAC) have risen sharply and it is now the predominant subtype in high-income countries². Patients with locally advanced EAC are treated with neoadjuvant chemotherapy (CTx) or radiochemotherapy (RCTx) followed by surgical resection³. Although neoadjuvant treatment confers a survival benefit over resection alone, 50–60% of tumors are resistant to neoadjuvant therapy,

leading to an overall poor outcome with a 5-year survival of less than 50% (refs. 3,4). Immune-checkpoint blocking treatments seem to have some potential in EAC^{5–7}, but have not revolutionized the standard of care in the perioperative setting⁸.

Despite the advances in perioperative treatment strategies for patients with EAC, the molecular understanding of both treatment resistance mechanisms and the modulating effect of neoadjuvant treatment are poorly understood. Translational studies showed that

A full list of affiliations appears at the end of the paper. ✉e-mail: melissa.barroux@mri.tum.de; trevor.graham@icr.ac.uk

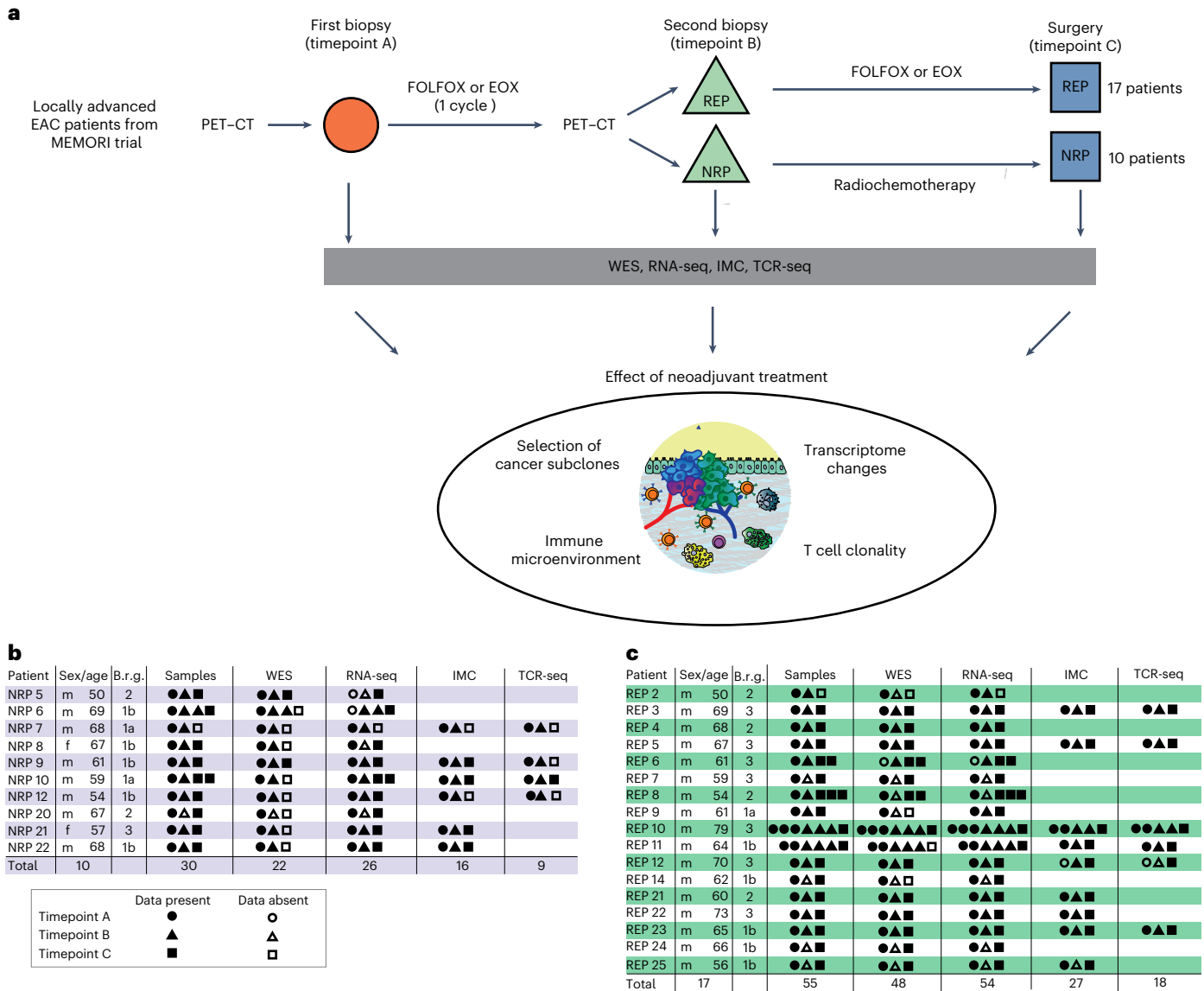


Fig. 1 | Experimental workflow and overview of the study cohort. a, Flowchart summarizing patient treatment and study design, including respective neoadjuvant treatment, sample acquisition and analyses. FOLFOX, oxaliplatin and 5-FU; EOX, epirubicin, oxaliplatin and capecitabine; WES, whole-exome sequencing; RNA-seq, RNA-sequencing; IMC, imaging mass cytometry;

TCR-seq, T cell receptor sequencing. **b, c**, Overview of the study cohort of NRPs (**b**) and REPs (**c**) with indication of samples present for each type of data analysis. Samples from different timepoints are indicated with different shapes. Age, age at diagnosis; Brg, Becker remission grade.

response to neoadjuvant treatment correlated with enrichment of lymphocytes, high immune-checkpoint molecules and p53 pathway enrichment in the treatment-naïve tumor⁹; however, longitudinal analyses to determine ecological and evolutionary dynamics, which could discriminate pre-existing and progressively developing factors leading to treatment resistance are lacking.

Sequencing studies have examined the genetic alterations in EACs during treatment to understand evolutionary dynamics that may lead to treatment resistance^{10–12}. The translational goal of these studies is to translate measures of the evolutionary dynamics into treatment-predictive biomarkers; however, there is growing evidence that genetic evolution alone does not fully explain resistance evolution¹³. Tumor plasticity, defined as cellular phenotype changes in the absence of underlying genetic change, is associated with treatment resistance in multiple cancer types^{14–16}. Furthermore, there is mounting evidence that the efficacy of chemotherapies also relies on activating antitumor immune responses¹⁷. Translational results from the PANDA trial highlighted measures of the tumor microenvironment (TME) as

an important predictor for response to combined immune-checkpoint blockade (ICB) and CTx in the neoadjuvant setting¹⁸.

There is a major practical challenge in collecting longitudinal samples over space and time from solid tumors, limiting the availability of this valuable data. Here we have performed multi-region, multi-timepoint whole-exome sequencing (WES) at high depth (mean 300×) of locally advanced EAC to identify mutations and track clonal dynamics across time and space, with matched RNA sequencing (RNA-seq) to characterize phenotype changes, and imaging mass cytometry (IMC) and T cell receptor (TCR) sequencing to characterize immune infiltrates and stromal cell dynamics. Our comprehensive analysis provides a holistic multiomic view of the dynamic changes in EAC and its microenvironment through neoadjuvant treatment.

Results

Longitudinal profiling in nonresponder and responder EAC EAC patients in the MEMORI trial¹⁹ underwent baseline ¹⁸F-FDG-PET (18-fluorodesoxyglucose positron emission tomography) followed by

one cycle of neoadjuvant platinum-based chemotherapy (CTx), with metabolic response assessed at day 14–21 by ^{18}F -FDG-PET. Responders (REPs; as shown by PET–CT scan) continued to receive chemotherapy, whereas nonresponders (NRPs) by PET–CT were switched to intensified radiochemotherapy (RCTx); for detailed information see Methods. The clinical trial outcomes have been fully reported previously¹⁹ and here we report on subsequent molecular genetic analyses of a completed trial. Of screened MEMORI patients, 13% ($n = 21$) were excluded due to no/low FDG uptake in the primary tumor¹⁹. FDG uptake intensity was not associated with global transcriptomic differences (Extended Data Fig. 1a), suggesting no major stratification in biologically different subgroups based on initial PET signal intensity. Pathological response in the post-treatment sample was assessed via tumor regression grades according to Becker²⁰. Overall, 70% of NRPs showed remission grade I, compared to only 35% of REPs (Extended Data Fig. 1b); however, despite the addition of RCTx leading to an augmented histological response rate, poor early metabolic response was still associated with inferior progression-free survival and overall survival (Extended Data Fig. 1c,d). Analogous results were reported in the AGITG DOCTOR trial²¹. Given that initial PET-measured metabolic response correlated with outcome, our study design therefore aimed to analyze ecological and evolutionary dynamics in REPs and NRPs to understand the cellular and molecular effect of different treatment modalities in EAC.

Longitudinal molecular analysis was performed on 10 NRPs and 17 REPs (Fig. 1a). From most patients, three cancer samples were collected: one pretreatment biopsy (timepoint A), one biopsy after the first cycle of platinum-based chemotherapy (timepoint B) and the surgical cancer resection specimen sample after completion of neoadjuvant treatment (timepoint C) (Fig. 1a–c). For two patients (REP10 and REP11) we performed more extensive multi-timepoint and multi-region sampling (≥ 6 samples per patient).

After clinical and histopathological review (Supplementary Table 1) all samples were microdissected (Methods) and whole-exome sequenced (22 tumor samples from NRPs and 48 tumor samples from REPs; at mean coverage of $300\times$ (range 44–478 \times) with matched blood germline control at mean coverage of 282 \times (Supplementary Table 2). We called single-nucleotide variants (SNVs), indels and copy number alterations (CNAs). Tumor cellularity was not significantly different between timepoints (Extended Data Fig. 2a). Matched bulk 3' RNA-seq was performed on 26 samples from NRPs and 54 samples from REPs (Supplementary Table 3). Immune composition during treatment was analyzed with a 21-marker IHC panel (39 regions of interest (ROIs) from 16 NRP samples and 74 ROIs from 27 REPs samples; Fig. 1b,c). Bulk TCR sequencing was performed on 18 samples from REPs and 9 samples from NRPs (Fig. 1b,c).

Limited evidence for clonal selection during treatment

We first assessed genetic changes in REPs and NRPs (Fig. 2a–c), finding an average mutational burden of 23.09 SNVs/Mb (range 7.5–127.7 SNVs per Mb) in treatment-naïve EAC, consistent with previous literature after accounting for our higher sequencing depth^{22,23}.

The overall SNV burden between pre- and post-treatment samples showed neither a significant difference in the overall cohort (Fig. 2a) nor when stratified by initial response (Fig. 2b).

Fig. 2 | Evolutionary dynamics of mutations during neoadjuvant treatment in EAC. a–c, Violin plots showing the distribution of mutational burden during neoadjuvant treatment for all patients (a), stratified by treatment response (b) and stratified by clonality of mutation (c). Mutations of each sample were classified as clonal or subclonal based on the copy number and cellularity adjusted cancer cell fraction. *P* values in a–c were calculated by the two-sided Wilcoxon test. **d**, Selected phylogenetic trees with clade length indicating the number of shared mutations between samples. Timepoint of samples are annotated at the tip of the clades with the letters A–C. Numbers at the nodes indicate bootstrap values. EAC drivers harboring SNVs (without brackets) or indels (in squared brackets) and number of neoantigenic SNVs are annotated on the clades of the trees. HI, homoplasy index; NeoSNVs, neoantigenic SNV.

We assessed changes in mutation clonality, reasoning that if treatment drove clonal selection, we might see increased clonal and/or subclonal mutational burden between pre- and post-treatment; however, no significant difference was detected for either mutation class (Fig. 2c), nor after stratifying by the treatment that was given (Extended Data Fig. 2b,c).

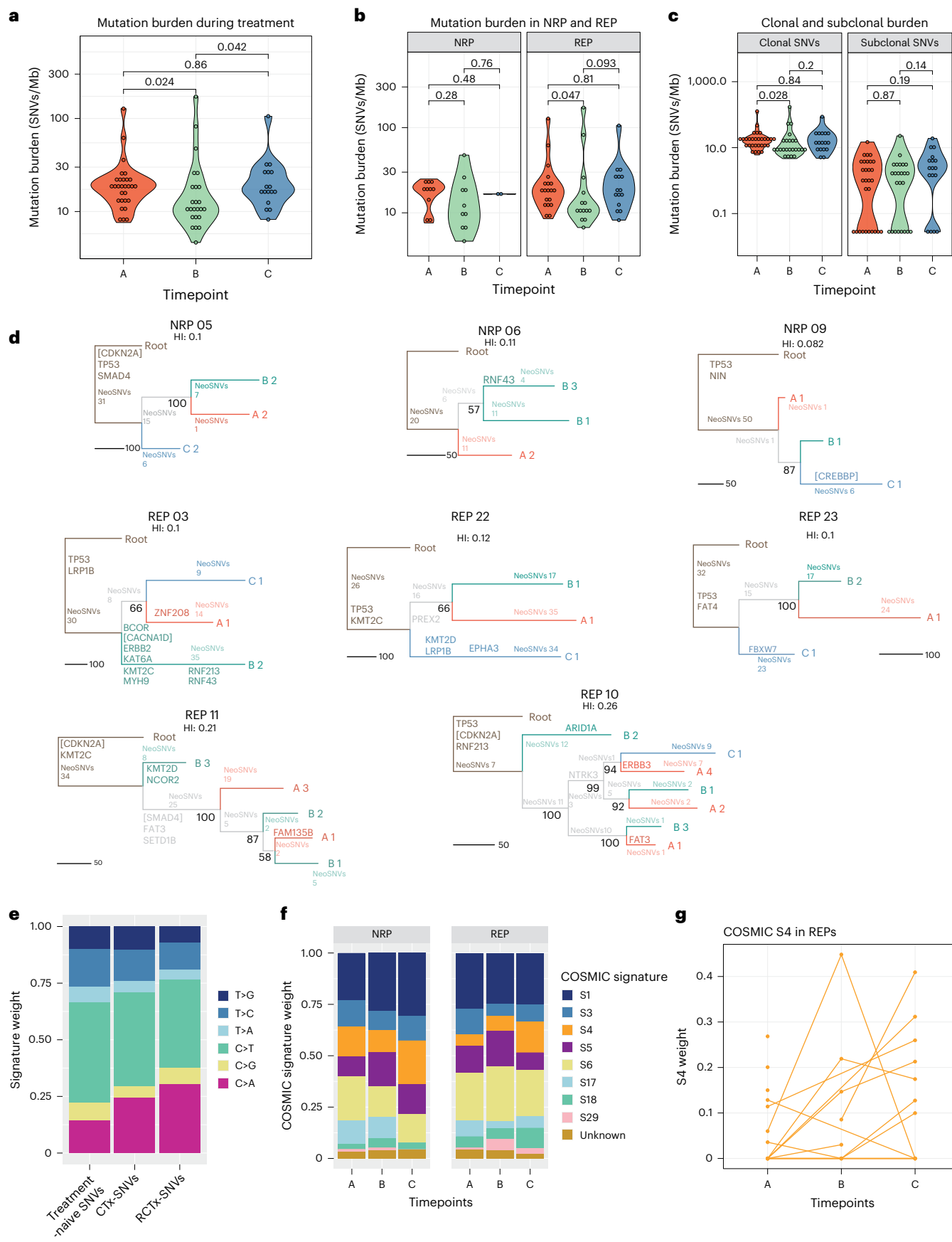
To probe clonal dynamics, we constructed SNV-based phylogenetic trees for 13 patients with multi-timepoint and multi-region samples (≥ 3 samples) (Fig. 2d and Extended Data Fig. 2d)²⁴. The majority of phylogenetic trees were visually ‘balanced’ with similar clade lengths for all samples. We observed progressive clonal sweeps during neoadjuvant treatment in only one sample (NRP9; Fig. 2d and Extended Data Fig. 2d). In all other cases, samples from timepoint C were either most similar to precursor clones of samples from timepoints A and B (for example REP22), or most similar to a clone detected at timepoint A (for example REP10). Notably, patients with multi-region sampling (REP10 and REP11) showed more similarity between samples from different timepoints than between multi-region samples. A parsimonious explanation of these observations is that the cancer was a mosaic of clones, and inferred clonal relationships between timepoints and/or spatial samples were determined by spatial sampling rather than by a clonal sweep driven by treatment.

Known high-frequency driver events such as *TP53* and *CDKN2A* were mostly truncal on the phylogenetic trees, indicating that these drivers persisted through treatment. *TP53* SNVs were present in 17 patients (Figs. 2d and 3e and Extended Data Fig. 2d) and *TP53* indels in 4 out of 27 patients (Figs. 2d and 3e and Extended Data Fig. 2d), with 14 out of 23 patients with ≥ 2 samples harboring clonal *TP53* alterations present in all samples. *CDKN2A* SNVs were present in two patients (Fig. 3e and Extended Data Fig. 2d) and *CDKN2A* indels in four patients (Figs. 2d and 3e) with clonal genetic *CDKN2A* alterations in 5 out of 23 patients with ≥ 2 samples (Figs. 2d and 3e), consistent with previous literature^{22,23,25,26}. We examined the phylogenetic trees from 11 patients with sequencing from pre- and post-treatment timepoints, finding in 6 patients that there were new low-frequency putative drivers (those mutated in $< 5\%$ of samples in IntOGen cohorts) post-treatment and in the remaining 5 patients there were no new drivers post-treatment. This suggests no major changes in the clonal make-up for the majority of patients during neoadjuvant treatment.

dN/dS analyses (the ratio of nonsynonymous to synonymous substitutions) to detect evidence of clonal selection of treatment induced SNVs showed dN/dS-1 for treatment-naïve and RCTx induced SNVs, indicating no evidence of selection. dN/dS of 0.8 (CI 0.7–0.96) for CTx-induced SNVs showed weak evidence of negative selection (Supplementary Table 5).

As distinct treatment regimens have been associated with specific mutational footprints²⁷, we computed mutational signatures for our cohort. SNVs from our phylogenetic trees were classified into treatment-naïve SNVs, SNVs acquired during chemotherapy exposure (CTx-SNVs) and SNVs acquired during RCTx exposure (RCTx-SNVs). Treatment-naïve SNVs, CTx-SNVs and RCTx-SNVs showed significant differences in their six-channel mutation signatures (chi-squared test $P < 0.001$), with an increase in C > A mutations during CTx,

e, Proportion of SNV types in treatment-naïve SNVs (left), SNVs occurring under chemotherapy (middle) and SNVs occurring under RCTx (right) from phylogenetic tree analyses. A, adenine; T, thymine; C, cytosine; G, guanine. $n = 5,341$ CTx-induced SNVs, $n = 283$ RCTx induced SNVs, $n = 9,787$ treatment-naïve SNVs. **f**, Proportion of COSMIC signatures in NRPs and REPs during treatment (COSMIC signature calling was limited to those with a weight $> 5\%$ in the respective groups). Samples from NRP: $n = 10$ at timepoint A, $n = 10$ at timepoint B, $n = 2$ at timepoint C; samples from REP: $n = 19$ at timepoint A, $n = 14$ at timepoint B, $n = 15$ at timepoint C. **g**, Line graph showing changes in the proportion of COSMIC signature 4 in responders during treatment. For multi-region samples means were plotted for each timepoint.



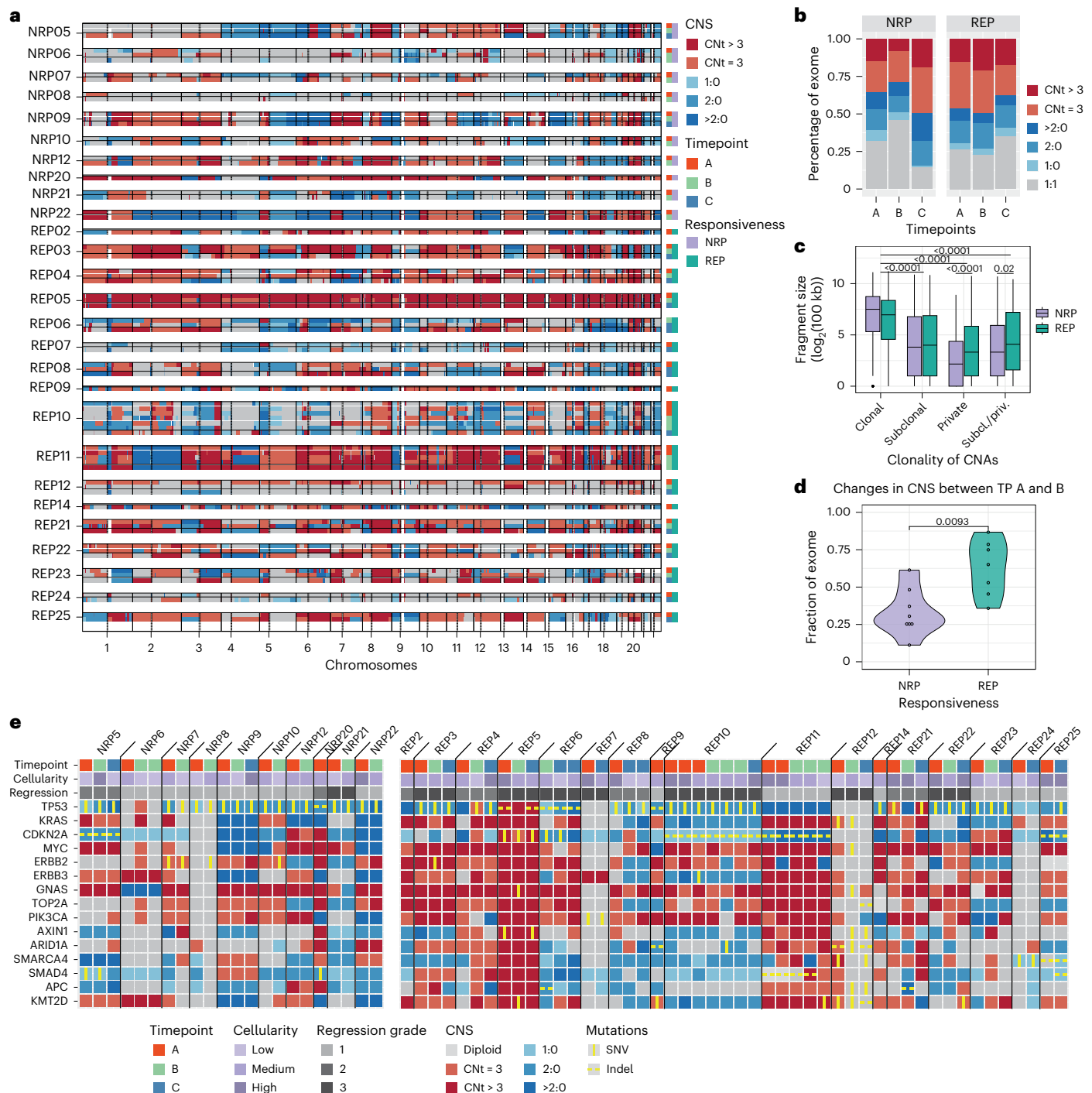


Fig. 3 | Dynamics in copy number alterations during neoadjuvant treatment. **a**, Plot showing genome-wide copy number state. Each row represents a sample, with samples from the same patient grouped together and patient ID is annotated on the left. Treatment response and timepoint of each sample are annotated on the right. Dashed vertical lines indicate the centromere of each chromosome and continuous vertical lines are separating different chromosomes. CNS, copy number state; CNT, copy number. **b**, Percentage of altered exome in REPs and NRPs during neoadjuvant treatment. CNS: copy number state. Samples from NRPs $n = 10$ at timepoint A, $n = 10$ at timepoint B, $n = 2$ at timepoint C; Samples from REPs: $n = 19$ at timepoint A, $n = 14$ at timepoint B, $n = 15$ at timepoint C. **c**, Fragment size of clonal, subclonal and private CNAs. Box plots show the median, two hinges representing the first and third quartiles and two whiskers showing the minimum and maximum. In patients with only two samples available, no distinction between subclonal and private could be made and therefore CNAs were summarized in 'subclonal/private' category. Number

of clonal fragments: $n = 281$ in REPs, $n = 180$ in NRPs. Number of subclonal fragments: $n = 315$ in NRPs, $n = 1,492$ in REPs; number of subclonal/private fragments $n = 460$ in NRPs, $n = 307$ in REPs; number of private fragments $n = 202$ in NRPs, $n = 995$ in REPs. P values are calculated by the two-sided Wilcoxon test. Subcl./priv., subclonal/private. **d**, Fraction of exome with changing copy number state between timepoint A and B in NRPs and REPs. P values are calculated by a two-sided Wilcoxon test. TP, timepoint. **e**, Plot shows genetic alterations, including CNAs, SNVs and indels for putative cancer driver genes identified by IntOGen. Each vertical column represents a sample. Samples of the same patients are grouped together and patient ID is annotated at the top. Information on timepoint, cancer cellularity and the patient's pathological regression grade treatment are found in the top three rows. The following rows show information on genetic alterations in EAC driver genes. Cellularity was defined as low (10–30%), medium (31–60%) or high (61–100%). Regression grades were evaluated by a pathologist according to Becker regression classification.

which is consistent with previously described platinum-induced mutation signatures^{10,11,27} (Fig. 2e). To further investigate this, we called 96-channel COSMIC signatures for all samples (Extended Data Fig. 2e). Across subgroups from different treatment response and timepoints, we detected eight prevalent COSMIC signatures (Fig. 2f), of which all have been previously identified in EAC^{9,12,28–31}. REPs showed a nonsignificant increase in S4 signature during treatment, which is dominated by C > A changes and thus most likely oxaliplatin driven²⁷ (Fig. 2f,g).

Copy number evolution through treatment

EAC genomes typically have high CNA burden^{23,28,32}; consistent with this our cases had median 69.4% genome altered (PGA, range 1.1–100%) (Fig. 3a). Copy number amplifications were seen frequently on chromosomes 1q, 3q, 5p, 7p, 8q, 19 and 20, while losses or loss of heterozygosity (LOH) predominated on chromosomes 3p, 4q, 5q, 9p and 17p, consistent with previous work^{10,28,33} (Fig. 3a).

Treatment-naïve tumors from REPs and NRPs displayed similar proportions of amplifications, deletions, loss and LOH (Fig. 3b). Chemotherapy did not increase PGA, whereas RCTx, known to cause broad single- or double-strand breaks, led to higher PGA (*t*-test *P* value = 0.03) (Fig. 3b). Segments that changed their copy number state during treatment were significantly smaller than fragments that were clonally altered (Fig. 3c). Furthermore, private CNAs were smaller in NRPs than in REPs (*t*-test *P* value < 0.001).

We examined whether CNA dynamics correlated with early treatment response in EAC. REPs showed significant changes in CNA burden with a mean of 63% (range 36–87%) of genome changing its copy number status after the first cycle of chemotherapy, whereas copy number states in NRPs were slightly more stable with a mean of 33% (range 11–61%) of genome altering copy number state (Wilcoxon rank-sum test *P* value 0.009; Fig. 3d). We speculate that NRPs may have genomes that confer pre-existing resistance to the effect of neoadjuvant chemotherapy, whereas REPs have profiles that confer chemotherapy sensitivity, therefore the first dose of chemotherapy prompts further alteration.

Genetic and transcriptomic dynamics in EAC drivers

We examined genetic alterations in 108 genes suggested to be drivers of EAC evolution (Supplementary Table 6 and Extended Data Fig. 3)^{33,34} and we show 15 common EAC driver genes in Fig. 3e. In 19 out of 27 patients, we observed that *TP53* LOH or loss co-occurred with *TP53* SNVs or indels, presumably leading to a loss of *TP53* function. *CDKN2A* showed copy number loss or LOH in 21 out of 27 patients, which co-occurred with SNVs or indels in 5 patients (consistent with literature²²). We observed amplifications containing *MYC*, *KRAS*, *ERBB2*, *ERBB3*, *GNAS*, *TOP2A* and *PIK3CA* and deletion of *SMAD4*. Of note, CNAs in driver genes were mostly present before treatment and persisted in their CNA category (amplification, LOH and loss) during treatment, although the exact copy number state could vary (Fig. 3e). Both REP and NRP showed no significant change in the burden of genomic alterations of driver genes during treatment (Extended Data Fig. 4a–f). REPs showed a mean of 85.3 genetically altered putative driver genes at timepoint A, 92.4 at B and 76.7 at timepoint C (Extended Data Fig. 4b). NRPs had a mean of

77.1 genetically altered putative drivers at timepoint A, 65.4 at B and 94.0 at timepoint C; however, we did not detect any specific cancer gene that was enriched for CNAs, SNVs or indels in REPs versus NRPs (Fig. 3e and Extended Data Fig. 3). We note that work in colorectal cancer has shown that mutations that are drivers ‘on average’ in a cohort may not be a driver in an individual cancer¹⁶, and the driver status of CNAs is unclear, so we do not claim that all these driver alterations are necessarily important for EAC evolution.

We next explored gene expression changes in high-frequency drivers using our matched RNA-seq data. Significant expression changes were observed for most driver genes: expression tended to increase for *GNAS*, *PIK3CA* and *SMAD4*, decrease for *ARID1A*, *CDKN2A*, *ERBB2*, *ERBB3*, *TOP2A*, *SMARCA4*, *KRAS* and *KMT2D* and was stable for *TP53*, *MYC*, *APC* and *AXIN1* (Extended Data Fig. 4g). We found little evidence that copy numbers drove expression, with correlations between copy number state and RNA expression in only a few genes (Extended Data Fig. 5a). Correlation analyses between SNVs in driver genes and their expression were only possible for *TP53* and *CDKN2A*, as analyses for other drivers were underpowered. We observed significantly higher *CDKN2A* expression in *CDKN2A* mutated samples and significantly lower *TP53* expression in *TP53* mutated samples (Extended Data Fig. 5b).

Neoadjuvant treatment alters the EAC transcriptome

We assessed gene and pathway expression changes during neoadjuvant treatment using RNA-seq in 26 samples from 10 NRPs and 54 samples from 17 REPs.

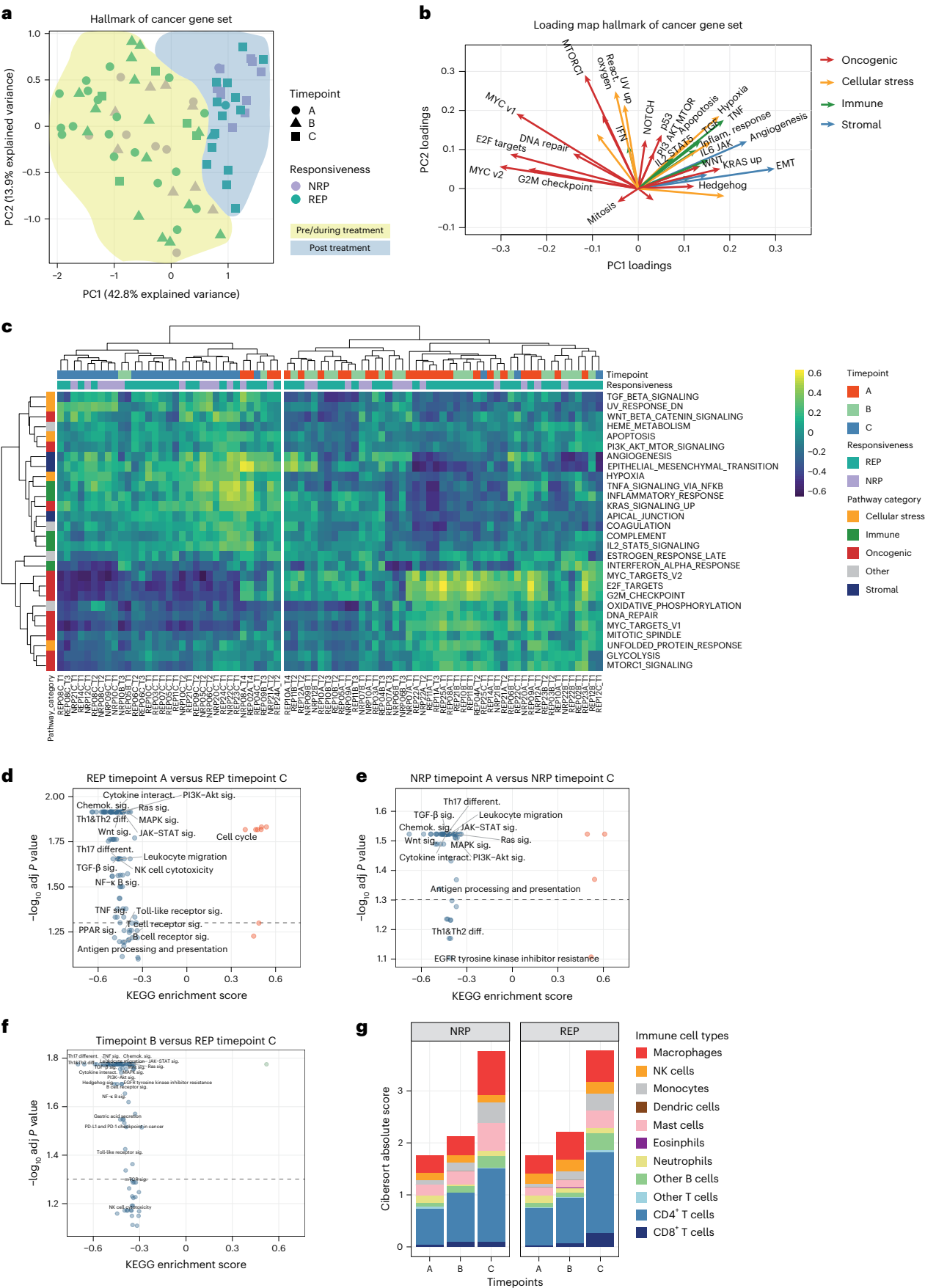
Principal-component analysis (PCA) using hallmark pathways³⁵ separated samples from timepoint A and B from timepoint C (Fig. 4a); however, samples from REPs and NRPs were intermixed. Most patients with multi-region sampling showed pre- and post-treatment samples clustering on the opposite sides of PC1, with samples from timepoint B found in between (Extended Data Fig. 5c), suggesting a gradual change of the transcriptome over time.

Hallmark pathways were grouped into ‘classes’ according to their biological function (‘oncogenic’, ‘immune’, ‘stromal’ and ‘cellular stress’)³⁶. PCA loading assessment showed that samples from timepoint A and B were enriched for oncogenic pathways, whereas samples from timepoint C were enriched in immune and stromal pathways as well as selected oncogenic pathways (*KRAS*, *Hedgehog* and *WNT* signaling; Fig. 4b). We identified hallmark genes that were on average significantly differentially expressed between pre/early-treatment samples and samples at the end of neoadjuvant treatment, and performed hierarchical clustering of all samples using these genes. Expectedly, and consistent with PCA analysis, the dendrogram separated into two groups (Fig. 4c): group 2, containing most samples from timepoint A/B, was enriched for ‘oncogenic’ acting pathways, such as *MYC*, cell cycle associated pathways, DNA repair and *MTORC* signaling (Fig. 4c); and group 1, including mostly samples from timepoint C, showed significant enrichment of epithelial–mesenchymal transition (EMT) and stemness-associated *WNT* signaling and promoters of stem cell-like state such as *TGF-β* signaling and hypoxia. Moreover, immune pathways such as *IL6* and *IL2* signaling and inflammatory response and oncogenic

Fig. 4 | Neoadjuvant treatment leads to profound changes in gene and pathway expression in EAC.

a, PCA of single sample gene set enrichment analysis of cancer hallmark gene sets. Background shading represents a visual highlight. PC, principal component. **b**, Principal-component feature loadings (magnitude and direction) from PCA in **a**. Vectors are colored according to their biological classification of cancer hallmark gene sets. **c**, Hierarchical clustering with heatmap showing the significantly differentially expressed pathways between the two clusters (right cluster is predominantly samples from timepoint A/B and left cluster is predominantly timepoint C). Sample IDs and timepoints are annotated at the bottom of the heatmap. **d**, Enrichment analyses in KEGG pathways in REPs between timepoint A and C. Samples from

REPs: *n* = 19 at timepoint A and *n* = 19 at timepoint C. **e**, Enrichment analyses in KEGG pathways in NRPs between timepoint A and C. Samples from NRPs: *n* = 8 at timepoint A and *n* = 10 at timepoint C. **f**, Enrichment analyses in KEGG pathways during chemotherapy (all samples at timepoint B versus REPs at timepoint C). Samples at timepoint B: *n* = 24 and REPs at timepoint C: *n* = 19. Dotted lines in **d–f** indicate significance level of *P*_{adj} < 0.05 (false discovery rate (FDR)-adjusted *P* values). **g**, Plot shows immune cell composition based on CIBERSORT analysis in REPs and NRPs during neoadjuvant treatment. Samples from NRPs: *n* = 8 at timepoint A, *n* = 8 at timepoint B, *n* = 10 at timepoint C; Samples from REPs: *n* = 19 at timepoint A, *n* = 16 at timepoint B, *n* = 19 at timepoint C. sig., significant; diff., differentiation.



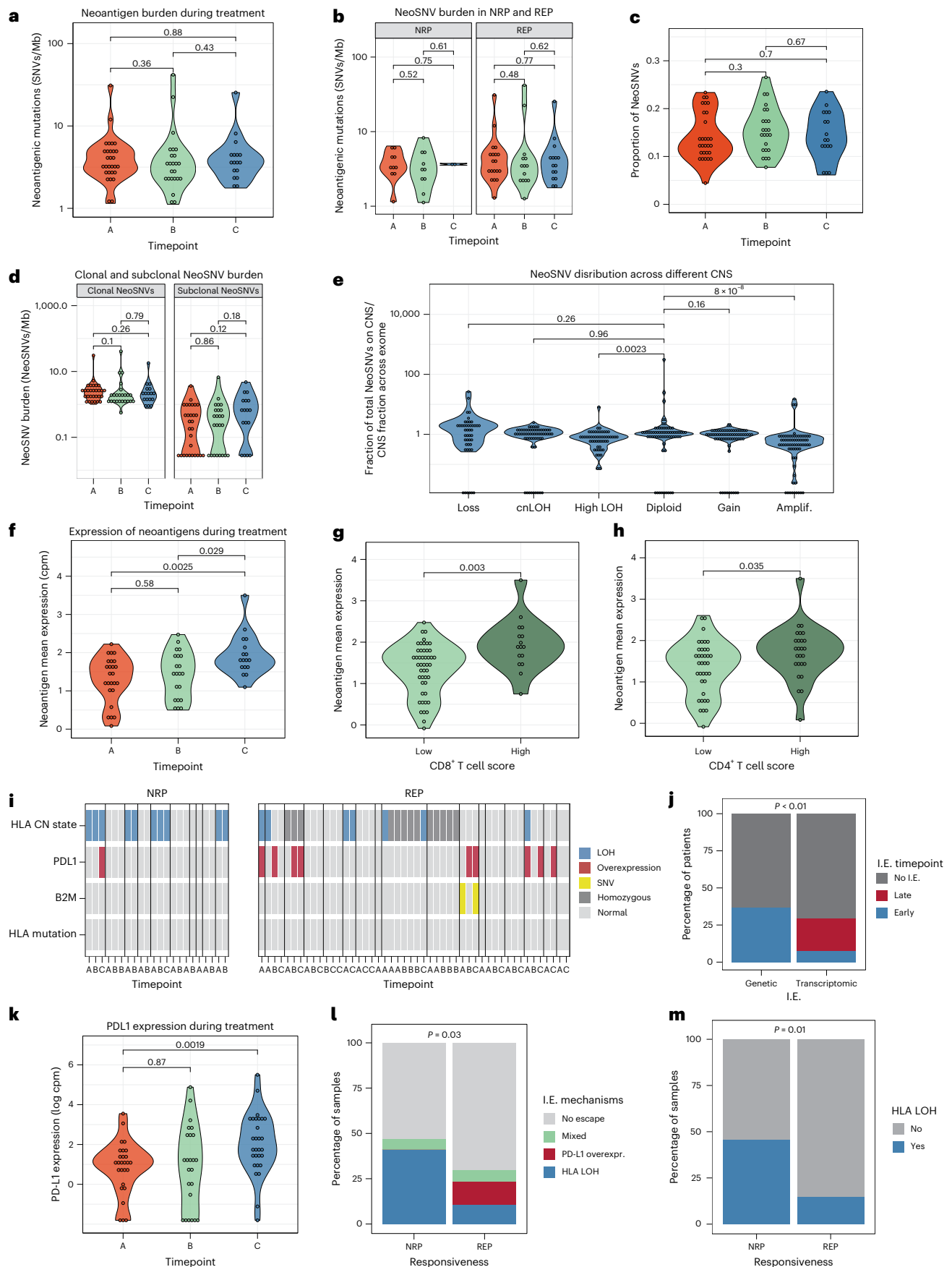


Fig. 5 | Increasing immune escape during neoadjuvant treatment correlates with poor treatment response. **a–d**, Violins showing the neoantigenic mutational burden during neoadjuvant treatment in all samples (**a**), stratified by treatment response (**b**), expressed as a proportion of total SNVs (**c**) and stratified by clonality (**d**). Clonal and subclonal neoantigenic mutational burden during neoadjuvant treatment. Mutations of each sample were classified as clonal or subclonal based on the copy number (CN) and cellularity-adjusted CCF. **e**, Distribution of neoantigenic SNVs based on their copy number states. The CN-normalized proportion of neoantigenic SNVs in each CN segment was calculated. **f**, Expression of neoantigens during treatment. **g,h**, Neoantigen expression in EAC according to immune infiltration score for CD8⁺ T cells (**g**) and CD4⁺ T cells (**h**). **i**, Presence of HLA-LOH, PD-L1 overexpression and *B2M* mutations in individual samples from NRPs (left) and REPs (right). Samples from individual patients are separated by vertical black lines. PD-L1 overexpression

was defined as PD-L1 expression >2 s.d. from the mean of all treatment-naïve samples. **j**, Proportion of early and late occurrence of genetic and nongenetic immune escape in cohort of *n* = 27 patients. Genetic immune escape refers to mutations or LOH in HLA or *B2M* mutations, whereas PD-L1 overexpression represents transcriptomic immune escape. *P* value calculated by the two-sided chi-squared test (*P* = 0.003). **k**, PD-L1 expression during neoadjuvant treatment. **l**, Proportion of immune escaped samples and their escape mechanism stratified by treatment response in NRPs (*n* = 17 samples) and REPs (*n* = 47 samples) with matching WES and RNA-seq data. **m**, Proportion of samples with HLA-LOH stratified by treatment response in NRPs (*n* = 22 samples) and REPs (*n* = 48 samples). *P* values in **j–m** are calculated by the two-sided chi-squared test. *P* values in all other panels are calculated by a two-sided Wilcoxon test, unless stated otherwise. Amplif., amplification; I.E., immune escape; overexpr., overexpression.

KRAS and *PI3K-AKT-MTOR* signaling were significantly enriched in the post-treatment group (Fig. 4c).

Pathway enrichment between pre- and post-treatment samples in REPs and NRPs showed significant upregulation of *WNT*, *PI3K*, *RAS*, *MAPK* and *JAK-STAT*, indicating that both chemotherapy and RCTx lead to major and similar transcriptomic changes in tumor cells (Fig. 4d,e). Immune-related pathways were also significantly altered during treatment in REPs (Fig. 4d,e). Further, there was significant upregulation of immune activation pathways in post-treatment samples after CTx (Fig. 4f and Extended Data Fig. 5d), whereas post-treatment samples after RCTx showed no significant changes in immune-related pathways.

We used immune deconvolution tools to delineate cellular composition changes from RNA-seq data. Using CIBERSORT³⁷, we observed a gradual increase in absolute numbers of immune cells during neoadjuvant treatment in REPs and NRPs (Fig. 4g); however, this may be due to lower tumor cellularity in post-treatment samples. Proportions of individual immune cell types stayed stable during treatment (Fig. 4g), with CD4⁺ and CD8⁺ cells comprising 40–50% of all immune cells. Other deconvolution tools (Consensus^{TME} and Syllolist) confirmed the gradual increase in immune infiltrates during treatment (Extended Data Fig. 6a,b) but there was variability in the estimated proportions of immune cell types.

In summary, cancer-relevant gene expression programs significantly changed during treatment, with enrichment of developmental programs such as EMT, stemness-associated *WNT* signaling and promoters of stem cell-like state such as *TGF-β* signaling and hypoxia, despite infrequent clonal replacement. Our data therefore suggest that cancer cells alter their phenotype without clonal replacement and that phenotypic plasticity might underlie these observations.

Immune escape correlates with treatment response

Neoantigens were called from WES data on 22 samples from 10 NRPs and 48 samples from 17 REPs. We did not observe any significant changes

in the neoantigenic mutation burden during neoadjuvant treatment (Fig. 5a,b and Extended Data Fig. 6c). Next we examined whether neoantigens were subject to selection (immune editing). We observed no change in proportions between immunogenic and total mutations during neoadjuvant treatment (Fig. 5c), indicating no enhanced negative selection of neoantigenic mutations during treatment. Subclonal neoantigenic mutational burden was not significantly different between pre- and post-treatment samples (Fig. 5d and Extended Data Fig. 6d) and most patients had comparable proportions of neoantigenic SNVs on the clades of their phylogenetic tree (Fig. 2d), indicating that neoantigenic subclones are not removed during treatment.

Next, we explored the relationship between CNAs and neoantigens. We hypothesized that gains of alleles carrying antigenic mutations were likely to experience negative selection, and so expected that gained alleles would be relatively depleted for neoantigens. To test this, we calculated the copy number-normalized proportion of neoantigens in each CNA segment. Diploid regions showed a ratio of -1, whereas gains (balanced and unbalanced) were significantly depleted for neoantigens and regions of copy number loss were weakly enriched for neoantigens (Fig. 5e).

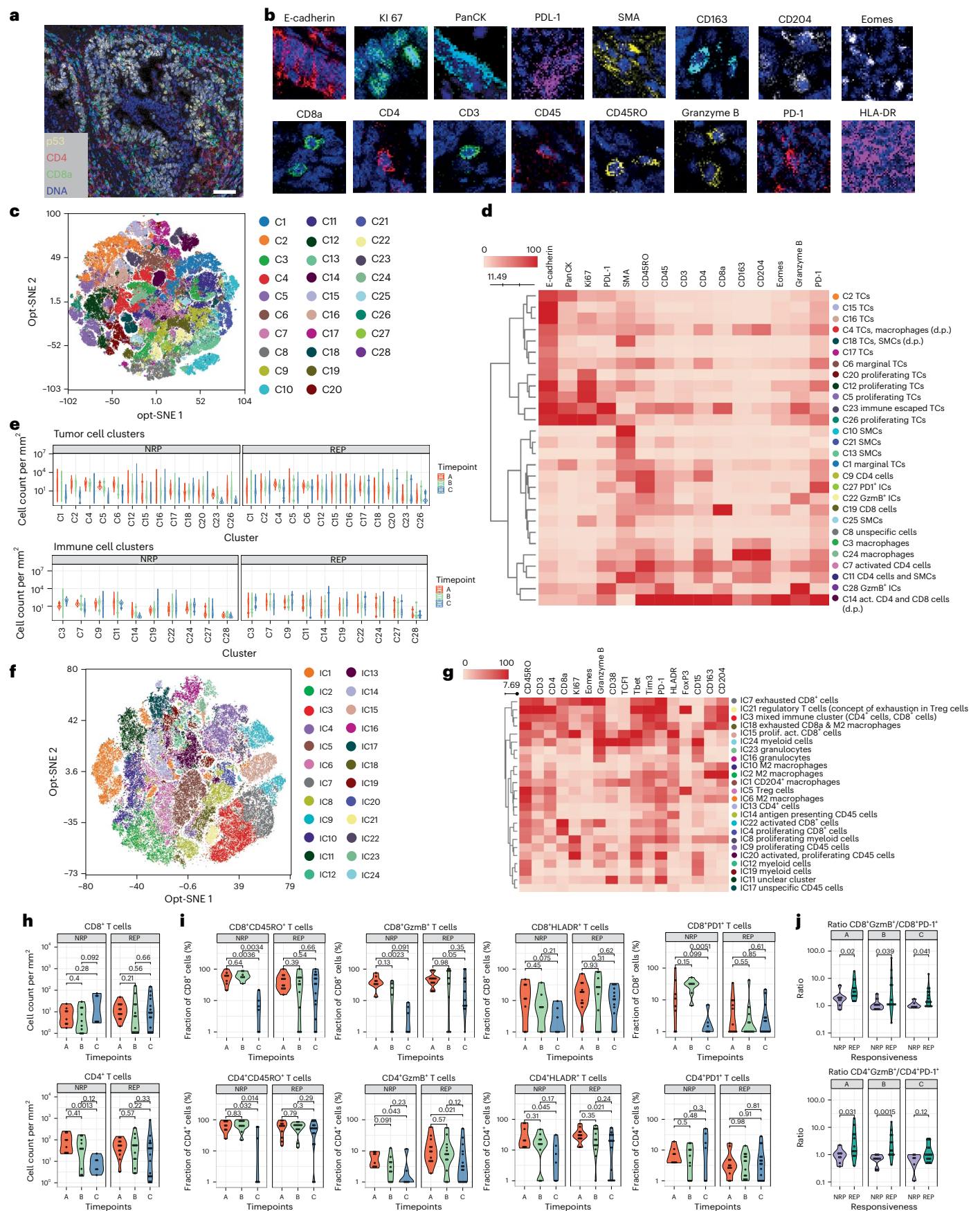
We hypothesized that transcriptional downregulation of neoantigens during treatment might also underlie immune evasion and potentially mediate treatment response. Counter to our hypothesis, we detected a significant increase in neoantigen expression during treatment (Fig. 5f). High neoantigen expression correlated with high CD8⁺ and CD4⁺ cell infiltration (Fig. 5g,h), suggesting that tumor cells with a high neoantigen expression were indeed recognized as ‘nonself’ and attracted immune cells. This can be explained if tumors subsequently develop stronger immune escape mechanisms during treatment or that the immune infiltrate becomes nonfunctional during treatment.

To test this, we first looked for tumor-cell-mediated immune escape mechanisms³⁸ (LOH or mutations in HLA, *B2M* mutations or programmed death-ligand 1 (PD-L1) and pathways or immune cells

Fig. 6 | Highly multiplexed imaging mass cytometry analysis reveals different T cell phenotype dynamics in NRPs and REPs during treatment.

a, Representative image IMC staining of EAC tissue. Scale bar, 100 μm. p53 (yellow), CD4 (red), CD8a (green) and DNA (blue) from IMC data channels are displayed. Representative IMC images were taken from a minimum of 15 ROIs across different samples. **b**, Representative IMC images of each marker together with DNA (blue). Representative IMC images for each marker were taken from a minimum of 15 ROIs across different samples. **c**, *t*-SNE visualization of the EAC tumor, stromal and immune map based on 28 identified cell clusters. **d**, Heatmap visualization of marker expression in the 28 cell clusters. Normalized median marker expression is shown. TCs, tumor cells; SMCs, smooth muscle cells; ICs, immune cells; act, activated; d.p., in direct proximity to each other; GzmB, Granzyme B. **e**, Cell cluster dynamics during treatment are shown for NRPs and REPs. Box plots show the median, two hinges representing the first and third quartiles and two whiskers showing the minimum and maximum. ROIs from NRPs (*n* = 8 at timepoint A, *n* = 10 at timepoint B, *n* = 6 at timepoint C). ROIs from REPs (*n* = 12 at timepoint A, *n* = 13 at timepoint B, *n* = 16 at

timepoint C). *P* values were calculated by a two-sided analysis of variance test. Exact *P* values: *P*(C1,NRP) = 0.0007, *P*(C2,NRP) < 0.0001; *P*(C4,NRP) = 0.0008; *P*(C5,NRP) < 0.0001; *P*(C6,NRP) = 0.0003; *P*(C23,NRP) < 0.0001; *P*(C26,NRP) = 0.02; *P*(C1,REP) = 0.02; *P*(C4,REP) < 0.0001; *P*(C5,REP) = 0.03; *P*(C6,REP) = 0.002; *P*(C12,REP) = 0.0005; *P*(C16,REP) = 0.007; *P*(C17,REP) = 0.04; *P*(C7,NRP) = 0.035; *P*(C14,NRP) = 0.03; *P*(C19,NRP) = 0.005; *P*(C19,REP) = 0.003. Unreported *P* values did not reach the significance level. **f**, *t*-SNE visualization of CD45⁺ cell map based on 24 identified cell clusters. **g**, Heatmap visualization of marker expression in the 24 CD45⁺ cell clusters. Normalized median marker expression is shown. **h**, Absolute CD4⁺ and CD8⁺ cell counts per mm² during treatment. **i**, T cell phenotypes in patients with EAC during treatment were analyzed for markers of T cell activation and exhaustion. Fractions of CD8⁺ cells (top row) and CD4⁺ cells (bottom row) were compared among patient groups and visualized by violin plots. **j**, Ratio of activated and exhausted CD8⁺ cells (top row) and CD4⁺ cells (bottom row) is shown during treatment for REPs and NRPs. *P* values in all other panels are calculated by the two-sided Wilcoxon test, unless stated otherwise.



associated with immune suppression). Genetic immune escape mechanisms such as HLA-LOH or *B2M* mutations were detected significantly more often before treatment (early), whereas transcriptomic PD-L1 overexpression occurred mostly during and after neoadjuvant treatment (late) (Fig. 5i–k). Increased expression of PD-L1 may represent a mechanism of rapid adaptation that is positively selected during treatment. Moreover, RNA-seq deconvolution revealed a significant increase in immune-suppressive M2-macrophages during treatment in NRPs and an increase in signaling pathways associated with immune suppression such as TGF- β , IL2-STAT5 and IL6-Jak-STAT3 signaling in both REPs and NRPs (Extended Data Fig. 6e–j).

We examined the correlation between immune escape and treatment response. Samples from NRPs were more often immune escaped than REPs, suggestive of a role for the immune system in potentiating the chemotherapy treatment response (Fig. 5l). The main immune escape mechanism in NRPs was HLA-LOH, occurring in 46% of NRPs and only in 13% of REPs (Fig. 5m). Our data suggest that immune escape has an important role in treatment resistance, highlighting that immunotherapy could help to circumvent resistance to standard treatment.

A distinct tumor microenvironment defines treatment response

We assessed the cellular organization of the immune microenvironment using multiplex IHC on 24 ROIs from 16 NRP samples and 42 ROIs from 27 REP samples. We quantified expression of 19 markers, representing canonical lymphoid and myeloid immune populations, together with tumor cell markers (Fig. 6a,b and Extended Data Fig. 6k).

First, we explored cellular phenotypes in EAC during neoadjuvant treatment. Taking a mean of 1.5 representative ROIs (range 1–3) from each timepoint we extracted single cell phenotype data for 533,734 cells and clustered cells using the phenograph algorithm³⁹, which identified 28 distinct cell populations (Fig. 6c). Based on molecular expression signatures, we identified phenotypically distinct populations of tumor cells (C1-2, C4-6, C12, C15–C18, C20, C23 and C26), immune cells (C3, C7, C9, C11, C14, C19, C22, C24 and C27–28) and other cell types (C8, C10, C13, C21 and C25; Fig. 6d). CD8⁺ T cells were common in C14 and C19, and CD4⁺ T cells in C7, C9, C11 and C14, and macrophages in C3 and C24 (Fig. 6d).

Dynamics in NRPs during treatment were dominated by a decrease in certain tumor cell populations (C1-2 and C4-6), decreases in the CD4⁺ cell population (C7), and the activated CD4 and CD8 cell cluster (C14) and an increase in one CD8⁺ cell population (C19) (Fig. 6e). REPs also showed decreasing abundances of tumor cell populations (C1, C4–C6, C12, C16 and C17) and increases in the same population of CD8⁺ cells (C19) (Fig. 6e). To further explore qualitative differences of the immune cell compartment we selected all leukocytes (CD45⁺ cells) and reclustered using only immune cell markers. This identified 24 distinct leukocyte subpopulations (Fig. 6f,g). We observed significant associations between T cell clusters and treatment timepoints for IC7, IC18, IC4, IC15 and IC3 (Extended Data Fig. 6l,m). NRPs showed a significant decrease in a mixed CD4/CD8 cluster (IC3) (Dunn-test $P = 0.01$) and in two exhausted CD8 clusters (IC7 and IC18) (Dunn-test $P = 0.001$ and $P = 0.01$, respectively). Both REPs and NRPs showed decreasing numbers of myeloid cells during treatment (Extended Data Fig. 6n).

Given their relevance to immunotherapy, we explored the dynamics of the CD8⁺ and CD4⁺ cells in more detail. NRPs showed stable CD8⁺ counts during treatment and a significant decrease in gated CD4⁺ cell counts, whereas their abundances stayed stable in REPs (Fig. 6h). We observed a strong decrease in CD4⁺ and CD8⁺ cell fractions expressing CD45RO in NRPs, indicating a loss of non-naïve T cells during RCTx (Fig. 6i), whereas in REPs these were stable (Fig. 6i). NRPs showed a significant drop in CD8⁺ cells expressing Granzyme B and in CD4⁺ cells expressing Granzyme B or HLA-DR (Fig. 6i), indicating a decrease in the effector T cell phenotype in NRPs. In contrast REPs showed a decrease in Granzyme B and HLA-DR expression in CD4⁺ cells, whereas

CD8⁺ cells stayed in their activated phenotype state during treatment (Fig. 6i). Exhausted CD8⁺ cells and CD4⁺ cells (expressing PD-1 or TIM-3) significantly decreased during RCTx in NRPs (Fig. 6i and Extended Data Fig. 7a,b). We calculated the ratio of CD4 and CD8 cells expressing Granzyme B⁺ (activated) vs those expressing PD-1 (exhausted) and found this was higher in REPs than NRPs at all timepoints (Fig. 6j), indicating a more cytotoxic T cell phenotype in REPs.

To assess the role of tumor heterogeneity, we examined an additional 47 multi-region ROIs from larger resection specimens (timepoint C). REPs and NRPs showed similar inter-region heterogeneity in CD4 and CD8 cell counts (Extended Data Fig. 7c); however, in REPs the range of CD4⁺ and CD8⁺ subsets found across multi-region ROIs was heterogeneous and broad, whereas in NRPs there was homogenous enrichment for nonactive subsets (Extended Data Fig. 7d–g). We observed that the treatment switch from CTx to RCTx led to a more exhausted T cell phenotype post-treatment, compared to the continuation of CTx alone (Extended Data Fig. 7h,i). We repeated TME analysis excluding post-treatment samples from the small number of patients with complete tumor remission ($n = 3$), and our findings were consistent with the full-cohort analysis, indicating that the detected changes are an antitumor response rather than tissue regeneration (Extended Data Fig. 8). Moreover, correlation with immune escape data, showed that samples with impaired neoantigen presentation due to HLA-LOH had a less-cytotoxic CD8⁺ and CD4⁺ cell phenotype than nonescaped samples (Extended Data Fig. 7j,k).

Dynamics of the T cell repertoire

The TCR repertoire, measurable by TCR sequencing, provides a way to assess the adaptive T cell immune response and was examined in 54 samples from nine patients through their treatment time course, including in cases with complete remission.

We observed an average of 296 total α TCR counts and 668 total β TCR counts in treatment-naïve NRPs and an average of 229 total α TCR counts and 380 total β TCR counts in treatment-naïve REPs, with a slight (nonsignificant) increase in total TCRs at the end of neoadjuvant treatment (Fig. 7a). The number of detected TCRs moderately correlated with the absolute T cell score from CIBERSORT ($R_{\alpha} = 0.5$, $R_{\beta} = 0.47$) (Fig. 7b).

We did not observe any differences in the overall shape of TCR clone size distribution during treatment exposure (Fig. 7c). We then focused on TCR clones that had significantly expanded between two timepoints, and observed early (starting between timepoint A and B) and persisting TCR expansions in REPs with good pathological regression (REP11 and REP23), while NRP10 and REP5 with poor response to CTx showed late (starting between timepoint B and C) and intermittent expansions (Fig. 7d and Extended Data Fig. 7l). We considered different thresholds of expansions, which were reactive to treatment and persisting through treatment (those expanding between timepoint A and C) in patients with data from all three timepoints, and the trend was consistent (Fig. 7e).

Next, we tracked T cell clone expansions during treatment in patients with different treatment response. REPs with poor pathological treatment response (Becker grade 3), showed significantly lower numbers of TCRs that expanded at least fourfold or at least eightfold between two timepoints during treatment than REPs and NRPs with excellent regression (Fig. 7f).

Discussion

This work describes our integrative genetic, transcriptomic and immune microenvironment analysis of longitudinal EAC samples taken before, during and after neoadjuvant treatment. Notably, we did not observe clonal replacement during neoadjuvant treatment; however, these results are in line with previous findings in a multi-region WES study of pre- and post-treatment EAC samples, which similarly reported clonal persistence with rarely new occurring putative drivers

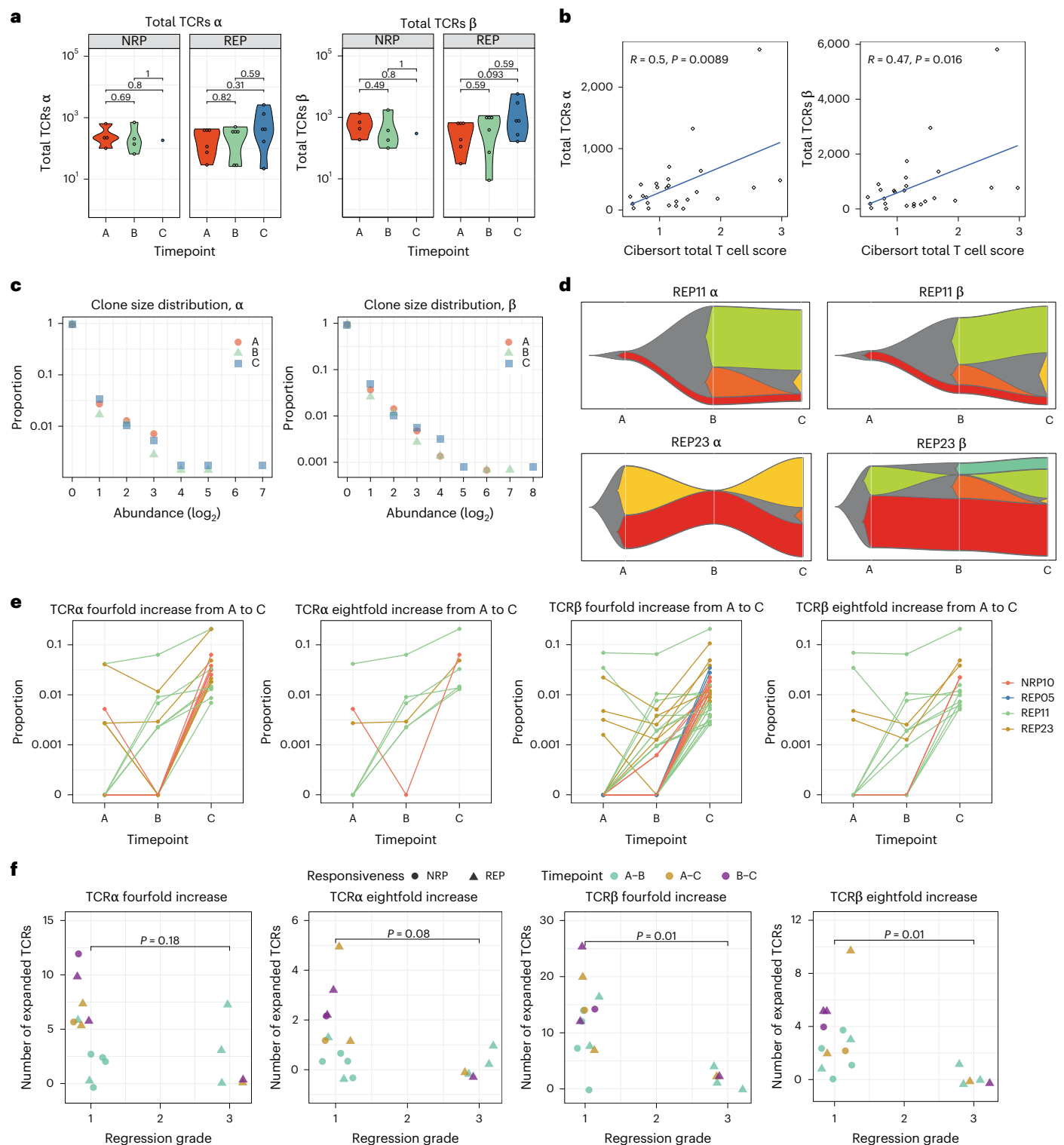


Fig. 7 | T cells show clonal expansion in patients with neoadjuvant treatment response. **a**, Numbers of total TCRs α -chain (left) and β -chain (right) in REPs and NRPs during treatment. P values are calculated by a two-sided Wilcoxon test. **b**, Correlation between TCR counts α -chain (left) and β -chain (right) and quantitative deconvolution of T cells from RNA-seq data via CIBERSORT. Two-tailed Pearson's correlation coefficients are reported in the plots. **c**, Abundance distribution profile of TCRs at timepoints A–C. The y axis shows the proportion of the TCRs that are found at the abundance indicated by

the x axis. **d**, Fishplots show the number of fourfold-expanded TCRs between any two timepoints REP11 (top) and REP23 (bottom). The colors correspond to the combination of timepoints that the TCR expansion occur in. **e**, The proportions of T cell clones that are expanded \geq fourfold and \geq eightfold between timepoint A and C. **f**, Numbers of TCRs expanded \geq fourfold and \geq eightfold during treatment periods (A–B, A–C and B–C), stratified by pathological regression grades. P values are calculated by a two-sided Mann–Whitney U -test.

post-treatment¹¹. We note that another study by Findlay et al. did report loss of mutations (and clones) through treatment¹⁰, but this could be explained by low cellularity in some of Findlay et al.'s post-treatment samples.

Recent evidence implicates a key role of nonmutational resistance mechanisms (where cells can plastically switch phenotype without underlying genetic change) in drug resistance^{14,15,40,41}. Here, we observed marked changes in transcriptional programs without clonal replacement during neoadjuvant treatment, which may be evidence of tumor cell plasticity. Although we emphasize that many mutations were gained and lost through the time course, our analyses cannot rule out that such phenotypic change is a consequence of genetic changes with underlying polyclonal evolution. Joint analysis of phenotype and genotype data showed major transcriptome and TME changes during treatment, whereas clonal changes were more minor, suggesting an actual change in the tumor's phenotype and TME during treatment rather than a consequence of sampling a heterogeneous tumor.

The enrichment of EMT gene expression programs in our post-treatment samples is consistent with previously reported plasticity of these programmes^{14,40,42}. Further, EMT is known to be controlled by multiple signaling pathways, such as *TGF-β*, *WNT*, *Notch* and *Ras-MAPK* pathways^{40,43,44}, which all showed a significant increase during treatment in EAC. The apparent readiness of EAC cells to undergo EMT in response to CTx and RTx via interleukin-6 upregulation, has also been shown in vitro⁴⁵ and is associated with poor prognosis⁹. We speculate that inhibition of the pathways that promote EMT, with the goal of maintaining cancer cells in a state susceptible to chemotherapy, could represent an avenue for future treatment strategies.

A high neoantigen burden is associated with good prognosis in patients with a variety of cancers^{46–48} and with successful immune-checkpoint therapy^{49–52}. Indeed, recently approved combined immuno-chemotherapy based on results from CheckMate 649 (ref. 53), Keynote-180 (ref. 5), Keynote-590 (ref. 6) and the CheckMate 577 trial⁷ showed a benefit for EAC in the metastatic and adjuvant setting. Keynote-585 investigated combined immunochemotherapy in the perioperative setting and showed higher rates of pathological complete response, but no improvement in the overall survival after treatment with combined immunochemotherapy compared to chemotherapy alone⁸. As the majority of patients with EAC do not respond adequately to immunotherapy, a better molecular characterization to predict response to CTx, RCTx and immunotherapy is essential.

We observed immune escape via genetic mechanisms and shifts to an immunosuppressive TME in NRPs. Further, cellular analysis showed remodeling of the T cell compartment during treatment, with expansion of T cell clones and a more activated T cell phenotype in patients with good treatment response. A previous study reported an association between actively proliferating CD8⁺ T cells and complete remission in EAC treated with neoadjuvant RCTx⁵⁴, and a further study found EACs with high lymphocyte and myeloid gene expression signatures before treatment had better OS⁵. Our data implicate a role for HLA-LOH in immune escape in NRPs. While HLA-LOH is associated with poor prognosis in a variety of cancer types^{55,56}, patients with disrupted tumor HLA-I presentation can still have durable responses to immunotherapy, especially when combined with a high tumor mutational burden^{57,58}. We note that our analysis of immune escape was not exhaustive; for example, alterations to the local metabolic environment and immune editing through epigenetic changes were not assessed.

We found that T cells remain in an active state during CTx, whereas RCTx causes a loss of cytotoxic T cell activity. Recently published work reported the predictive value of baseline CD8⁺PD-1⁺ T cell infiltrations and the increase of CD8⁺ cells after exposure to ICB for treatment response to neoadjuvant immunochemotherapy in EAC¹⁸. Collectively, these data offer an explanation for the results of the PERFECT trial, which showed that the combination of atezolizumab (PD-L1 inhibition) and neoadjuvant RCTx is only beneficial for patients with an already

inflamed microenvironment and that RCTx is not able to adequately reshape the immune landscape⁵⁹.

We note that PET-negative primary tumors were excluded from our study and represented 13% of the original screening MEMORI cohort. As primary tumors with different PET signal intensities did not show marked differences in their global transcriptomes, we suggest that our findings might be independent of the metabolic activity of the primary tumor, but future studies including PET-negative tumors will be required for validation.

In conclusion, our longitudinal multiomic study shows limited evidence of clonal replacement during neoadjuvant treatment in EAC but potent modulation of the immune cell compartment. These data motivate exploration of combination immunochemotherapy treatments in the neoadjuvant setting for EAC.

Methods

Prospective sample collection within clinical MEMORI trial

EAC specimens were obtained from the prospective clinical MEMORI trial (EudraCT 2014-000860-16)¹⁹. The performed translational research complies with the protocol of the MEMORI study, which was approved by the local ethics committee at Technical University Munich. All patients gave written informed consent for collection and molecular analysis of their sample material and the inclusion of the information listed in the manuscript within the MEMORI trial protocol. The study protocol is available on request.

Patients with locally advanced EAC and intense FDG tracer uptake of the tumor at baseline FDG-PET-CT (¹⁸F)-FDG uptake in the tumor at baseline $>1.35 \times$ liver standardized uptake value (SUV) $+ 2 \times$ s.d. of the liver SUV) and thus suitable for monitoring and early response prediction by FDG-PET were eligible for MEMORI trial. From 160 screened patients, 85 patients (53%) were excluded due to previously undetectable metastases ($n = 39$, 24%), no or too low FDG uptake of the primary tumor ($n = 21$, 13%) or other reasons ($n = 25$, 16%). All patients in the MEMORI trial received one cycle of platinum-based chemotherapy. A total of 23 patients received FOLFOX (oxaliplatin-5-FU) and 5 patients received EOX (epirubicin, oxaliplatin and capecitabine) for their first cycle of neoadjuvant chemotherapy. Metabolic tumor response was assessed with a repeated PET-CT at day 14–21. Responders in PET-CT scan (REPs) were defined as $\geq 35\%$ decrease in maximal SUV (SUV_{max}) from baseline and were continued on three more cycles of FOLFOX (d14) or four more cycles of EOX if EOX was given at the first cycle. Patients with poor response ($< 35\%$ decrease in SUV_{max} from baseline) were classified as NRPs and were switched to intensified RCTx (41.4 Gy/23 fractions with weekly carboplatin/paclitaxel) according to the CROSS protocol⁶⁰. Following completion of neoadjuvant treatment, restaging was performed. In the absence of progression to metastatic/unresectable disease, patients underwent surgical resection. Histopathological regression grade was assessed in the resection specimens after completion of neoadjuvant treatment. In this study sample, major histological response (Becker grade I) was achieved in 35% of REPs and 70% of NRPs (Extended Data Fig. 1b). Ten NRPs and 17 REPs were enrolled for longitudinal molecular analyses. Most patients provided three cancer samples with one pretreatment biopsy (timepoint A), one biopsy collected after the first cycle of chemotherapy (timepoint B) and the surgical specimen sample after completion of neoadjuvant treatment (either CTx or RCTx) (timepoint C) (Fig. 1b,c). No statistical methods were used to predetermine sample sizes but our sample sizes are similar to those reported in previous publications^{10,11,18}. Two patients (REP10 and REP11) had multi-timepoint and multi-region samples (≥ 6 samples per patient). Further clinical and histopathological information is provided in Supplementary Table 1.

Tumor tissue was fixed and stabilized with the PAXgene fixation method (PAXgeneTissue FIX Container (QIAGEN)). For eight samples formalin-fixed tissue was used (Supplementary Table 7). Post-treatment resection specimens showing Becker remission grade

1a (complete response) were excluded from genetic analyses, but included for immune analyses (RNA-seq and IHC). For post-treatment samples with remission grade 1b, 2 or 3, the remaining tumor cells were microdissected before DNA extraction, and included if genetic analysis showed EAC-like CNAs or SNVs. Blood for germline control was collected in PAXgene Blood DNA Tubes (QIAGEN). Data collection and analysis were not performed blind to the clinical subgroups of the experiments. Our longitudinal molecular analysis is based on samples from the MEMORI trial; however, the clinical trial's predefined primary and secondary outcomes are not subject to our molecular work. We report information on patients' sex in Fig. 1 and Supplementary Table 1. Sex and gender were not considered in the study design. Information on gender was not collected and is therefore not reported. Consent has been obtained for sharing individual-level data. Post hoc sex- and gender-based analysis were not performed as the study design is insufficient for sex- and gender-based analysis due to the small sample size.

Section preparation

PAXgene-fixed paraffin-embedded (PFPE) or formalin-fixed paraffin-embedded (FFPE) tissue were sectioned as follows; one section at 4 µm for hematoxylin and eosin (H&E) stain, eight sections at 10 µm onto PEN Membrane Glass Slides (Thermo Fisher) for subsequent isolation of DNA and RNA, four sections at 4 µm for IHC analysis and a final 4-µm section for a second H&E. Both H&Es were reviewed by a board-certified pathologist to assure high tissue quality and tumor cellularity. If tumor cellularity was estimated <50%, tumor areas were annotated for tumor cell enrichment. Sections for DNA extraction were stored at -20 °C and sections for RNA extractions at -80 °C, if not processed immediately.

DNA and RNA isolation. To increase cellularity, samples with <50% tumor cells were stained with methyl green and tumor cells enriched via laser capture microdissection using a PALM MicroBeam (Carl Zeiss Microscopy). DNA was extracted using the PAXgeneTissue DNA kit (QIAGEN) for PFPE tissue and the High Pure FFPE DNA Isolation kit (Roche Molecular Systems) for FFPE tissue according to the manufacturer's instructions. DNA from blood was extracted with the QIAamp DNA Blood Mini kit (QIAGEN). The integrity of DNA molecules was assessed via D5000 TapeStation Assay (Life Technologies). Samples with a total DNA yield higher than 10 ng and DNA peak detection at >1,000 bp were taken forward for WES library preparation.

RNA extractions from PFPE sections were performed using the PAXgeneTissue RNA kit from QIAGEN according to the manufacturer's protocol. For FFPE sections, RNA was extracted using the High Pure FFPE RNA Isolation kit (Roche Molecular Systems). RNA quantity was measured using the Qubit fluorometer RNA High Sensitivity assay (Life Technologies). Quality control was performed using the High Sensitivity RNA TapeStation system (Agilent). RNA quality was assessed using the DV200 value. RNA samples with a DV200 > 50% were eligible for further analysis.

Preparation of whole-exome sequencing libraries. Libraries were prepared using the SureSelectXT Low Input Target Enrichment System with Dual Indexing (Agilent Technologies) according to manufacturer's instructions. A short mechanical fragmentation step using a Covaris S2 Sonicator to generate 150–200-bp long fragments was performed and 8–14 PCR cycles were used for library enrichment depending on the DNA input. After purification, libraries were quantified by Qubit and run on the Agilent TapeStation using the HSD1000 assay. Samples with sufficient library DNA yield and characteristic fragment size distribution (-200–500 bp) were further subjected to deep (-300× depth) WES.

Preparation of RNA-seq libraries. Libraries were prepared using the QuantSeq 3' mRNASeq Library Prep kit FWD (Lexogen), according to the manufacturer's protocol with minor modifications. To increase the

total RNA library yields, the pre-PCR incubation time was increased to 1 h. After purification, libraries were quantified by Qubit and run on the Agilent TapeStation using the D1000 assay. Samples with sufficient library cDNA yield and characteristic fragment size distribution (-170–700 bp) were further subjected to RNA-seq.

WES and RNA sequencing. Sequencing libraries were multiplexed and sequenced on an Illumina Novaseq, typically using S2 flow cells. Read length and depth were varied as required by library composition. Target depth for WES was 250× and >2 million reads per sample for RNA-seq. Sequencing was performed by the Genome Centre at Queen Mary University London.

IHC staining. IHC staining was performed on 54 PAXgene-fixed samples and 12 FFPE samples (Supplementary Table 7). Incubation, rehydration and epitope retrieval was performed on 4-µm-thick tissue sections as described in previous work⁶¹. The sections were then stained with a mix of metal-labeled primary antibodies (Supplementary Table 4) diluted in TBS with 0.5% BSA and incubated at 4 °C overnight. Antibody binding conditions were determined in previous work^{61–64}. Sections were then rinsed, stained with Iridium Cell-ID and air-dried as previously described⁶¹. Slides were stored at room temperature until image acquisition.

IHC image acquisition. A 1–2-mm² image per sample was acquired using a Hyperion Imaging System (Fluidigm). Tuning of the instrument was performed according to the manufacturer's instructions. ROIs were determined based on a pathologist's annotations on consecutive H&E-stained section of each sample. A total of 66 ROIs were scanned as the exploratory set and 47 ROIs were scanned during the revision process for validation purposes and tumor heterogeneity analyses (Supplementary Table 7). Tissue sections were laser-ablated spot-by-spot at 200 Hz, resulting in a pixel 2 size/resolution of 1 mm. Preprocessing of the raw data was conducted using the CyTOF software v.7.0. Image acquisition control was performed using MCD Viewer v.1.0.560.6. For larger samples multiple ROIs were obtained.

TCR sequencing. Full details for both the experimental TCR-seq library preparation and the subsequent computational analysis (V, J and CDR3 annotation) using Decombinator are published in our previous work^{65,66}.

Bioinformatics summary methods

Detailed computational methods are described at <https://doi.org/10.17504/protocols.io.j8nlk9xpww5r/v1> (ref. 67). We note that bioinformatics scripts to reproduce our workflow are provided at https://github.com/meli3349/MEMORI_multioomics_data_analyses/tree/analysis, which includes descriptions of all software parameters used.

WES computational methods. Raw sequence data were quality-controlled and aligned following the GATK best practice pipeline^{68–70}. CNAs were called with Sequenza⁷¹, SNVs with Mutect⁷² and clonal inference performed with MOBSTER²⁴. Mutations were annotated by ANNOVAR⁷³ and drivers identified from the IntOGen database³⁴. Phylogenetic trees were constructed with Phangorn⁷⁴. Mutational signatures were computed with deconstructSigs⁷⁵. HLA typing was performed with Optitype⁷⁶ and neoantigens identified with NeoPredPipe⁷⁷.

RNA-seq computational methods. Basic RNA processing was performed with the STAR pipeline⁷⁸, and differential expression analysis with DESeq2 (ref. 79). Immune deconvolution analysis was performed with CIBERSORT³⁷.

Image mass cytometry computational methods. Basic processing was performed with the pipeline provided by the Bodenmiller group at <https://github.com/BodenmillerGroup/ImcSegmentationPipeline>.

Downstream analysis was performed with the OMIQ commercial software.

Statistics and reproducibility

No statistical method was used to predetermine sample size. Data distribution was assumed to be normal but this was not formally tested. The experiments were not randomized. The investigators were not blinded to allocation during experiments and outcome assessment. Of screened MEMORI patients, 13% ($n = 21$) were excluded due to no/low FDG uptake in the primary tumor¹⁹. RNA-seq data for samples that contained $<1.5 \times 10^6$ reads were excluded for further downstream analysis. Samples that did not show EAC-like CNAs or EAC-specific SNVs were excluded from genetic analyses.

Reporting summary

Further information on research design is available in the Nature Portfolio Reporting Summary linked to this article.

Data availability

Gene expression data, somatic mutation calls (MuTect2 and Annovar), copy number calls (Sequenza), neoantigen calls (Nepred pipeline) and called TCRs are available on Mendeley at <https://doi.org/10.17632/brsxy4746.1> (ref. 80). MCD files and cell segmentation files (IMC analyses) have been deposited at Zenodo at <https://doi.org/10.5281/zenodo.12800339> (ref. 81). Sequencing data have been deposited at the European Genome-phenome Archive (EGA), under accession numbers (EGAS50000000240 and EGAS50000000242). Access to these bam files is controlled and subject to application via the EGA platform. The accession of bam files is limited to research purposes and regulated with a data use agreement. The timeframe for response to requests is expected within 10 working days. Further information about the EGA can be found at <https://ega-archive.org>. Source data are provided with this paper.

Code availability

Complete scripts to replicate all bioinformatic analysis are available at https://github.com/meli3349/MEMORI_multiomics_data_analyses/tree/analysis.

References

- Sung, H. et al. Global cancer statistics 2020: GLOBOCAN estimates of incidence and mortality worldwide for 36 cancers in 185 countries. *CA Cancer J. Clin.* <https://doi.org/10.3322/caac.21660> (2021).
- Morgan, E. et al. International trends in oesophageal cancer survival by histological subtype between 1995 and 2014. *Gut* **70**, 234–242 (2021).
- Davies, A. R. et al. Tumor stage after neoadjuvant chemotherapy determines survival after surgery for adenocarcinoma of the esophagus and esophagogastric junction. *J. Clin. Oncol.* **32**, 2983–2990 (2014).
- Al-Batran, S. E. et al. Perioperative chemotherapy with fluorouracil plus leucovorin, oxaliplatin, and docetaxel versus fluorouracil or capecitabine plus cisplatin and epirubicin for locally advanced, resectable gastric or gastro-oesophageal junction adenocarcinoma (FLOT4): a randomised, phase 2/3 trial. *Lancet* **393**, 1948–1957 (2019).
- Shah, M. A. et al. Efficacy and safety of pembrolizumab for heavily pretreated patients with advanced, metastatic adenocarcinoma or squamous cell carcinoma of the esophagus: the phase 2 KEYNOTE-180 study. *JAMA Oncol.* **5**, 546–550 (2019).
- Sun, J. M. et al. Pembrolizumab plus chemotherapy versus chemotherapy alone for first-line treatment of advanced oesophageal cancer (KEYNOTE-590): a randomised, placebo-controlled, phase 3 study. *Lancet* **398**, 759–771 (2021).
- Kelly, R. J. et al. Adjuvant nivolumab in resected esophageal or gastroesophageal junction cancer. *N. Engl. J. Med.* **384**, 1191–1203 (2021).
- Shitara, K. et al. Neoadjuvant and adjuvant pembrolizumab plus chemotherapy in locally advanced gastric or gastro-oesophageal cancer (KEYNOTE-585): an interim analysis of the multicentre, double-blind, randomised phase 3 study. *Lancet Oncol.* **25**, 212–224 (2024).
- Naeini, M. M. et al. Multi-omic features of oesophageal adenocarcinoma in patients treated with preoperative neoadjuvant therapy. *Nat. Commun.* **14**, 3155 (2023).
- Findlay, J. M. et al. Differential clonal evolution in oesophageal cancers in response to neo-adjuvant chemotherapy. *Nat. Commun.* **7**, 11111 (2016).
- Murugaesu, N. et al. Tracking the genomic evolution of esophageal adenocarcinoma through neoadjuvant chemotherapy. *Cancer Discov.* **5**, 821–831 (2015).
- Noorani, A. et al. A comparative analysis of whole genome sequencing of esophageal adenocarcinoma pre- and post-chemotherapy. *Genome Res.* **27**, 902–912 (2017).
- Marine, J. C., Dawson, S. J. & Dawson, M. A. Non-genetic mechanisms of therapeutic resistance in cancer. *Nat. Rev. Cancer* **20**, 743–756 (2020).
- Boumahdi, S. & de Sauvage, F. J. The great escape: tumour cell plasticity in resistance to targeted therapy. *Nat. Rev. Drug Discov.* **19**, 39–56 (2020).
- Shaffer, S. M. et al. Rare cell variability and drug-induced reprogramming as a mode of cancer drug resistance. *Nature* **546**, 431–435 (2017).
- Househam, J. et al. Phenotypic plasticity and genetic control in colorectal cancer evolution. *Nature* **611**, 744–753 (2022).
- Galluzzi, L., Buque, A., Kepp, O., Zitvogel, L. & Kroemer, G. Immunological effects of conventional chemotherapy and targeted anticancer agents. *Cancer Cell* **28**, 690–714 (2015).
- Verschuur, Y. L. et al. Neoadjuvant atezolizumab plus chemotherapy in gastric and gastroesophageal junction adenocarcinoma: the phase 2 PANDA trial. *Nat. Med.* <https://doi.org/10.1038/s41591-023-02758-x> (2024).
- Lorenzen, S. et al. PET-directed combined modality therapy for gastroesophageal junction cancer: results of the multicentre prospective MEMORI trial of the German Cancer Consortium (DKTK). *Eur. J. Cancer* **175**, 99–106 (2022).
- Becker, K. et al. Histomorphology and grading of regression in gastric carcinoma treated with neoadjuvant chemotherapy. *Cancer* **98**, 1521–1530 (2003).
- Barbour, A. P. et al. Preoperative cisplatin, fluorouracil, and docetaxel with or without radiotherapy after poor early response to cisplatin and fluorouracil for resectable oesophageal adenocarcinoma (AGITG DOCTOR): results from a multicentre, randomised controlled phase II trial. *Ann. Oncol.* **31**, 236–245 (2020).
- Ross-Innes, C. S. et al. Whole-genome sequencing provides new insights into the clonal architecture of Barrett's esophagus and esophageal adenocarcinoma. *Nat. Genet.* **47**, 1038–1046 (2015).
- Dulak, A. M. et al. Exome and whole-genome sequencing of esophageal adenocarcinoma identifies recurrent driver events and mutational complexity. *Nat. Genet.* **45**, 478–486 (2013).
- Caravagna, G. et al. Subclonal reconstruction of tumors by using machine learning and population genetics. *Nat. Genet.* **52**, 898–907 (2020).
- Weaver, J. M. J. et al. Ordering of mutations in preinvasive disease stages of esophageal carcinogenesis. *Nat. Genet.* **46**, 837–843 (2014).

26. Nones, K. et al. Genomic catastrophes frequently arise in esophageal adenocarcinoma and drive tumorigenesis. *Nat. Commun.* **5**, 5224 (2014).
27. Pich, O. et al. The mutational footprints of cancer therapies. *Nat. Genet.* **51**, 1732–1740 (2019).
28. Secrier, M. et al. Mutational signatures in esophageal adenocarcinoma define etiologically distinct subgroups with therapeutic relevance. *Nat. Genet.* **48**, 1131–1141 (2016).
29. Noorani, A. et al. Genomic evidence supports a clonal diaspora model for metastases of esophageal adenocarcinoma. *Nat. Genet.* **52**, 74–83 (2020).
30. Alexandrov, L. B. et al. The repertoire of mutational signatures in human cancer. *Nature* **578**, 94–101 (2020).
31. Abbas, S. et al. Mutational signature dynamics shaping the evolution of esophageal adenocarcinoma. *Nat. Commun.* **14**, 4239 (2023).
32. Cancer Genome Atlas Research, N. et al. Integrated genomic characterization of oesophageal carcinoma. *Nature* **541**, 169–175 (2017).
33. Frankell, A. M. et al. The landscape of selection in 551 esophageal adenocarcinomas defines genomic biomarkers for the clinic. *Nat. Genet.* **51**, 506–516 (2019).
34. Gonzalez-Perez, A. et al. IntOGen-mutations identifies cancer drivers across tumor types. *Nat. Methods* **10**, 1081–1082 (2013).
35. Liberzon, A. et al. The Molecular Signatures Database (MSigDB) hallmark gene set collection. *Cell Syst.* **1**, 417–425 (2015).
36. Jimenez-Sanchez, A. et al. Unraveling tumor-immune heterogeneity in advanced ovarian cancer uncovers immunogenic effect of chemotherapy. *Nat. Genet.* **52**, 582–593 (2020).
37. Chen, B., Khodadoust, M. S., Liu, C. L., Newman, A. M. & Alizadeh, A. A. Profiling tumor infiltrating immune cells with CIBERSORT. *Methods Mol. Biol.* **1711**, 243–259 (2018).
38. Lakatos, E. et al. Evolutionary dynamics of neoantigens in growing tumors. *Nat. Genet.* **52**, 1057–1066 (2020).
39. Levine, J. H. et al. Data-driven phenotypic dissection of AML reveals progenitor-like cells that correlate with prognosis. *Cell* **162**, 184–197 (2015).
40. Quintanal-Villalonga, A. et al. Lineage plasticity in cancer: a shared pathway of therapeutic resistance. *Nat. Rev. Clin. Oncol.* **17**, 360–371 (2020).
41. Horn, L. A., Fousek, K. & Palena, C. Tumor plasticity and resistance to immunotherapy. *Trends Cancer* **6**, 432–441 (2020).
42. Arozarena, I. & Wellbrock, C. Phenotype plasticity as enabler of melanoma progression and therapy resistance. *Nat. Rev. Cancer* **19**, 377–391 (2019).
43. Thiery, J. P., Acloque, H., Huang, R. Y. & Nieto, M. A. Epithelial-mesenchymal transitions in development and disease. *Cell* **139**, 871–890 (2009).
44. Stemmler, M. P., Eccles, R. L., Brabletz, S. & Brabletz, T. Non-redundant functions of EMT transcription factors. *Nat. Cell Biol.* **21**, 102–112 (2019).
45. Ebbing, E. A. et al. Stromal-derived interleukin 6 drives epithelial-to-mesenchymal transition and therapy resistance in esophageal adenocarcinoma. *Proc. Natl Acad. Sci. USA* **116**, 2237–2242 (2019).
46. Balachandran, V. P. et al. Identification of unique neoantigen qualities in long-term survivors of pancreatic cancer. *Nature* **551**, 512–516 (2017).
47. Brown, S. D. et al. Neo-antigens predicted by tumor genome meta-analysis correlate with increased patient survival. *Genome Res.* **24**, 743–750 (2014).
48. Matsushita, H. et al. Neoantigen load, antigen presentation machinery, and immune signatures determine prognosis in clear cell renal cell carcinoma. *Cancer Immunol. Res.* **4**, 463–471 (2016).
49. Le, D. T. et al. PD-1 blockade in tumors with mismatch-repair deficiency. *N. Engl. J. Med.* **372**, 2509–2520 (2015).
50. Snyder, A. et al. Genetic basis for clinical response to CTLA-4 blockade in melanoma. *N. Engl. J. Med.* **371**, 2189–2199 (2014).
51. McGranahan, N. et al. Clonal neoantigens elicit T cell immunoreactivity and sensitivity to immune checkpoint blockade. *Science* **351**, 1463–1469 (2016).
52. Rizvi, N. A. et al. Cancer immunology. Mutational landscape determines sensitivity to PD-1 blockade in non-small cell lung cancer. *Science* **348**, 124–128 (2015).
53. Janjigian, Y. Y. et al. First-line nivolumab plus chemotherapy versus chemotherapy alone for advanced gastric, gastro-oesophageal junction, and oesophageal adenocarcinoma (CheckMate 649): a randomised, open-label, phase 3 trial. *Lancet* **398**, 27–40 (2021).
54. Goedegebuure, R. S. A. et al. Pre-treatment tumor-infiltrating T cells influence response to neoadjuvant chemoradiotherapy in esophageal adenocarcinoma. *Oncoimmunology* **10**, 1954807 (2021).
55. McGranahan, N. et al. Allele-specific HLA loss and immune escape in lung cancer evolution. *Cell* **171**, 1259–1271 e1211 (2017).
56. Zhou, Y. F. et al. Integrated analysis reveals prognostic value of HLA-I LOH in triple-negative breast cancer. *J. Immunother. Cancer* <https://doi.org/10.1136/jitc-2021-003371> (2021).
57. Anagnostou, V. et al. Multimodal genomic features predict outcome of immune checkpoint blockade in non-small-cell lung cancer. *Nat. Cancer* **1**, 99–111 (2020).
58. Rodig, S. J. et al. MHC proteins confer differential sensitivity to CTLA-4 and PD-1 blockade in untreated metastatic melanoma. *Sci. Transl. Med.* <https://doi.org/10.1126/scitranslmed.aar3342> (2018).
59. van den Ende, T. et al. Neoadjuvant chemoradiotherapy combined with atezolizumab for resectable esophageal adenocarcinoma: a single-arm phase II feasibility trial (PERFECT). *Clin. Cancer Res.* **27**, 3351–3359 (2021).
60. Shapiro, J. et al. Neoadjuvant chemoradiotherapy plus surgery versus surgery alone for oesophageal or junctional cancer (CROSS): long-term results of a randomised controlled trial. *Lancet Oncol.* **16**, 1090–1098 (2015).
61. Schwabenland, M. et al. Deep spatial profiling of human COVID-19 brains reveals neuroinflammation with distinct microanatomical microglia-T-cell interactions. *Immunity* **54**, 1594–1610 e1511 (2021).
62. Ijsselstein, M. E., van der Breggen, R., Farina Sarasqueta, A., Koning, F. & de Miranda, N. A 40-marker panel for high dimensional characterization of cancer immune microenvironments by imaging mass cytometry. *Front. Immunol.* **10**, 2534 (2019).
63. Schlecht, A. et al. Imaging mass cytometry for high-dimensional tissue profiling in the eye. *BMC Ophthalmol.* **21**, 338 (2021).
64. Sade-Feldman, M. et al. Defining T cell states associated with response to checkpoint immunotherapy in melanoma. *Cell* **175**, 998–1013 e1020 (2018).
65. Uddin, I. et al. Quantitative analysis of the T cell receptor repertoire. *Methods Enzymol.* **629**, 465–492 (2019).
66. Oakes, T. et al. The T cell response to the contact sensitizer paraphenylenediamine is characterized by a polyclonal diverse repertoire of antigen-specific receptors. *Front. Immunol.* **8**, 162 (2017).
67. Barroux, M. et al. MEMORI-Methods for computational analyses. *protocols.io* <https://doi.org/10.17504/protocols.io.j8nlk9xpwwr/v1> (2025).
68. Van der Auwera, G. A. et al. From FastQ data to high confidence variant calls: the Genome Analysis Toolkit best practices pipeline. *Curr. Protoc. Bioinformatics* **43**, 11 10 11–11 10 33 (2013).

69. McKenna, A. et al. The Genome Analysis Toolkit: a MapReduce framework for analyzing next-generation DNA sequencing data. *Genome Res.* **20**, 1297–1303 (2010).
70. DePristo, M. A. et al. A framework for variation discovery and genotyping using next-generation DNA sequencing data. *Nat. Genet.* **43**, 491–498 (2011).
71. Favero, F. et al. Sequenza: allele-specific copy number and mutation profiles from tumor sequencing data. *Ann. Oncol.* **26**, 64–70 (2015).
72. Cibulskis, K. et al. Sensitive detection of somatic point mutations in impure and heterogeneous cancer samples. *Nat. Biotechnol.* **31**, 213–219 (2013).
73. Wang, K., Li, M. & Hakonarson, H. ANNOVAR: functional annotation of genetic variants from high-throughput sequencing data. *Nucleic Acids Res.* **38**, e164 (2010).
74. Schliep, K. P. phangorn: phylogenetic analysis in R. *Bioinformatics* **27**, 592–593 (2011).
75. Rosenthal, R., McGranahan, N., Herrero, J., Taylor, B. S. & Swanton, C. DeconstructSigs: delineating mutational processes in single tumors distinguishes DNA repair deficiencies and patterns of carcinoma evolution. *Genome Biol.* **17**, 31 (2016).
76. Szolek, A. et al. OptiType: precision HLA typing from next-generation sequencing data. *Bioinformatics* **30**, 3310–3316 (2014).
77. Schenck, R. O., Lakatos, E., Gatenbee, C., Graham, T. A. & Anderson, A. R. A. NeoPredPipe: high-throughput neoantigen prediction and recognition potential pipeline. *BMC Bioinform.* **20**, 264 (2019).
78. Dobin, A. et al. STAR: ultrafast universal RNA-seq aligner. *Bioinformatics* **29**, 15–21 (2013).
79. Love, M. I., Huber, W. & Anders, S. Moderated estimation of fold change and dispersion for RNA-seq data with DESeq2. *Genome Biol.* **15**, 550 (2014).
80. Barroux, M. MEMORI_multiomic_data', Mendeley Data, V1 <https://doi.org/10.17632/brsxvy4746.1> (2024).
81. Barroux, M. et al. Imaging mass cytometry analysis of oesophageal adenocarcinoma during neoadjuvant treatment. *Zenodo* <https://doi.org/10.5281/zenodo.12800339> (2025).

Acknowledgements

The authors thank all patients and their families, nurses, study coordinators and investigators for their participation in the MEMORI study. The MEMORI trial was funded by the German Cancer Consortium (DKTK). The authors acknowledge funding from German Cancer Aid Society (Mildred-Scheel-Programm from Deutsche Krebshilfe) (M. Barroux), Bavarian Cancer Research Center (BZKF) (M. Barroux), Cancer Research UK (M. Barroux, A.B. and T.A.G.), the US National Institutes of Health via the Cancer Systems Biology Consortium U54 scheme (CA217376) (T.A.G.), the Thornton Foundation (T.A.G.), German Research Foundation (DFG; 3772/1) (M.Q.), Associazione Italiana Ricerca sul Cancro (AIRC) under MFAG 2020 (ID. 24913 project) (G.C.), DKTK (J.T.S.), DFG (405344257 (SI 1549/3–2)) (J.T.S.) and German Federal Ministry of Education and Research (01KD2206A/SATURN3) (J.T.S.). The MEMORI trial was supported by the DKTK. The authors acknowledge DKTK Partner site Essen, DKTK Partner site Freiburg, DKTK Partner site München. The authors thank K. Steiger and K.-P. Janssen at MRI for their excellent biobanking efforts and M. Angele (from Klinikum Großhadern d. LMU München) and S. Kasper-Virchow (from Westdeutsches Magen-und Darmzentrum Essen, Universitätsklinikum Essen) for their collaboration. The authors acknowledge iBioTUM-Tissue and study coordinator J.-P. Zimmermann for management of biosamples. The authors thank I. Rauscher and W. Weber (Department for Nuclear Medicine at TUM University Hospital), Wolfgang Fendler (Department for Nuclear Medicine at Klinikum Großhadern d. LMU München) and Ken Herrmann (Clinic for

Nuclear Medicine at University Hospital Essen) for their assessment of treatment response in the MEMORI cohort.

Author contributions

M. Barroux conceived the translational project of the MEMORI study, generated data, analyzed and interpreted the data, with focus on WES data, RNA-seq and IMC data and wrote the manuscript. J.H. performed the raw data processing from fastq to bam files for WES data and RNA-seq data and supported M. Barroux with data analyses. E.L. analyzed the data with focus on neoantigen and immune escape data. T.R. analyzed and interpreted the data, with focus on TCR-seq data. S.N. contributed to CNA. A.M.B. contributed to data generation and to manuscript writing. M.M., K. Smith, C.K., A.B., V.G. and M. Borgmann contributed to data generation, M.J. performed histopathological analysis. G.C. performed MOBSTER-analyses L.Z. and E.G. contributed to dN/dS analyses K. Steiger, J.S.-H., S. Lorenzen, S. Liffers, M.A., H.F., W.W. and R.M.S. contributed to clinical data and sample collection and sample coordination. B.C. contributed to TCR-seq data generation. H.S. and B.B. contributed to IMC data generation, IMC data analyses and interpretation. J.T.S. designed and led the clinical MEMORI trial. M.Q. and T.A.G. conceived the study design, supervised the study, interpreted results and contributed to manuscript writing. M. Barroux, M.Q. and T.A.G. acquired funding for the study.

Competing interests

J.T.S. receives honoraria as a consultant or for continuing medical education presentations from AstraZeneca, Bayer, Boehringer Ingelheim, Bristol Myers Squibb, Immunocore, iMEDICO, MSD, Novartis, Roche/Genentech and Servier. His institution receives research funding from Abalos Therapeutics, Boehringer Ingelheim, Bristol Myers Squibb, Celgene, Eisbach Bio and Roche/Genentech; he holds ownership in FAPI Holding. K. Steiger is named on a patent on a radiopharmaceutical compound and serves as advisory board member for TRIMT GmbH; not related to the current work. M.Q. receives honoraria as consultant or for continuing medical education presentations from AstraZeneca, Bayer, Bristol-Myers Squibb, MSD Sharp Dohme, Novartis, Roche and Servier. T.A.G., B.C. and A.M.B. are named as co-inventors on patent applications that describe a method for TCR sequencing (GB2305655.9) and T.A.G. is named on a patent application for a method to measure evolutionary dynamics in cancers using DNA methylation (GB2317139.0). T.A.G. has received an honorarium from Genentech and consultancy fees from DAiNA Therapeutics. The remaining authors declare no competing interests.

Additional information

Extended data is available for this paper at <https://doi.org/10.1038/s43018-025-00955-w>.

Supplementary information The online version contains supplementary material available at <https://doi.org/10.1038/s43018-025-00955-w>.

Correspondence and requests for materials should be addressed to Melissa Barroux or Trevor A. Graham.

Peer review information *Nature Cancer* thanks Sarah Derks and Timothy Frankel for their contribution to the peer review of this work.

Reprints and permissions information is available at www.nature.com/reprints.

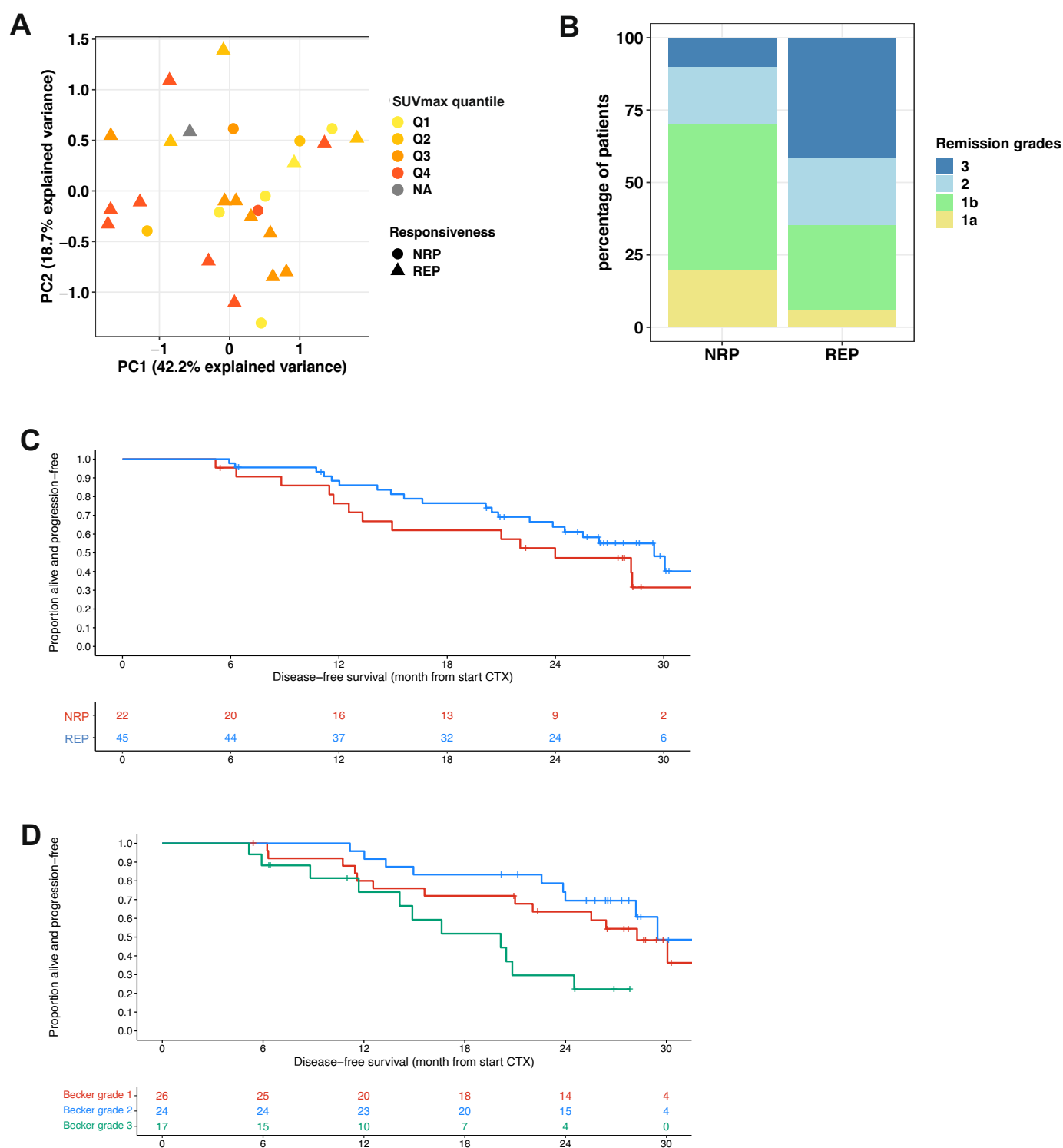
Publisher's note Springer Nature remains neutral with regard to jurisdictional claims in published maps and institutional affiliations.

Open Access This article is licensed under a Creative Commons Attribution-NonCommercial-NoDerivatives 4.0 International License, which permits any non-commercial use, sharing, distribution and reproduction in any medium or format, as long as you give appropriate credit to the original author(s) and the source, provide a link to the Creative Commons licence, and indicate if you modified the licensed material. You do not have permission under this licence to share adapted material derived from this article or parts of it. The images or other third party material in this article are included in the

article's Creative Commons licence, unless indicated otherwise in a credit line to the material. If material is not included in the article's Creative Commons licence and your intended use is not permitted by statutory regulation or exceeds the permitted use, you will need to obtain permission directly from the copyright holder. To view a copy of this licence, visit <http://creativecommons.org/licenses/by-nc-nd/4.0/>.

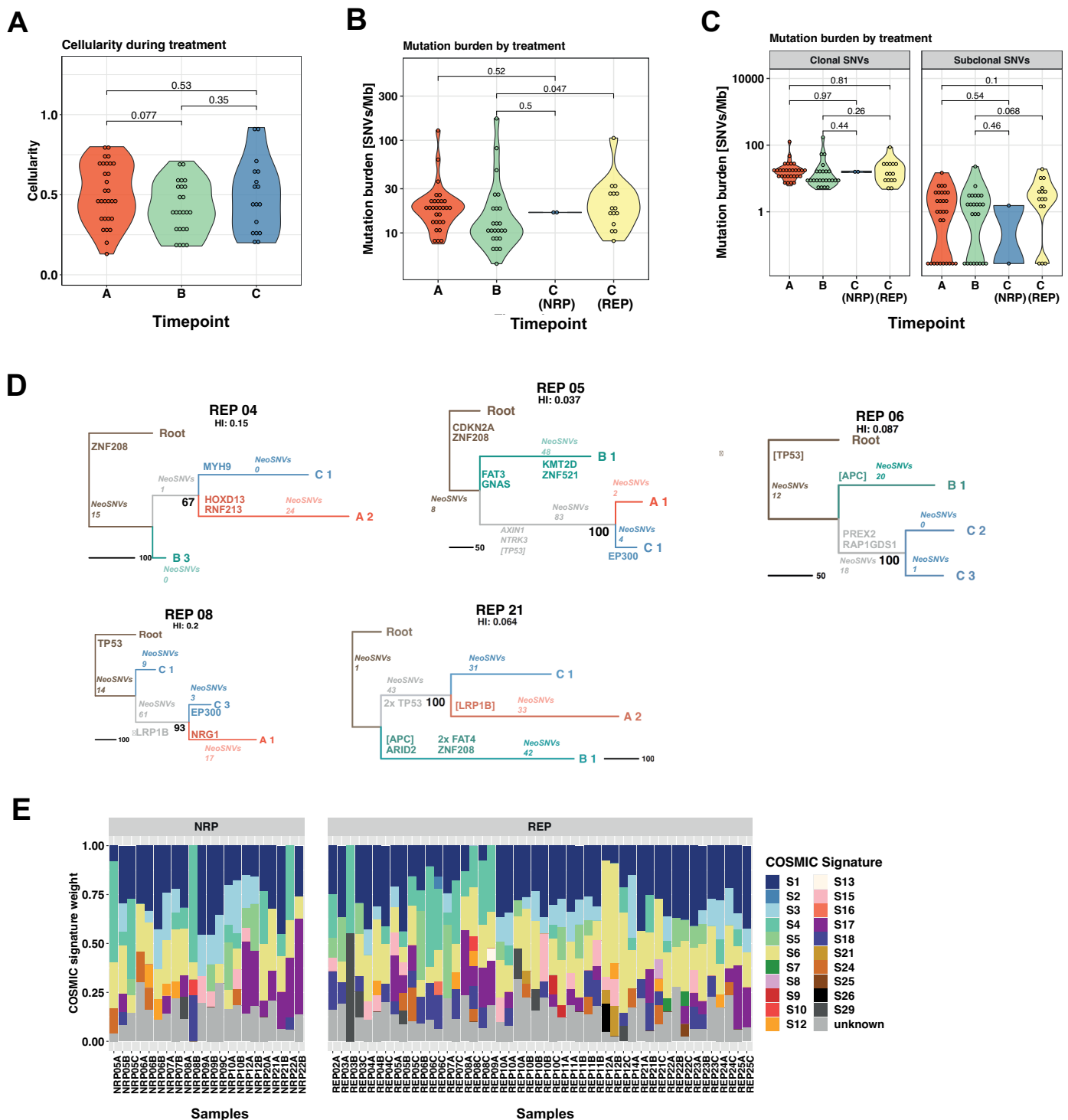
© The Author(s) 2025

¹Evolution and Cancer Laboratory, Centre for Genomics and Computational Biology, Barts Cancer Institute, Queen Mary University of London, London, UK. ²Medical Clinic and Polyclinic II, TUM University Hospital, Klinikum rechts der Isar, Munich, Germany. ³German Cancer Consortium (DKTK) Heidelberg, Germany, Partner Site Munich, Munich, Germany. ⁴Data Science Team, The Institute of Cancer Research, London, UK. ⁵Centre for Evolution and Cancer, The Institute of Cancer Research, London, UK. ⁶Division of Infection and Immunity, University College London, London, UK. ⁷Clinic for Internal Medicine II, University Medical Center Freiburg, Freiburg, Germany. ⁸Department of Pathology, UCL Cancer Institute, University College London, London, UK. ⁹Bridge Institute of Experimental Tumor Therapy (BIT), Division of Solid Tumor Translational Oncology (DKTK) and Department of Medical Oncology, West German Cancer Center, University Hospital Essen, University of Duisburg-Essen, Essen, Germany. ¹⁰German Cancer Consortium (DKTK), partner site Essen, a partnership between German Cancer Research Center (DKFZ) and University Hospital Essen, Essen, Germany. ¹¹Department of Mathematics, Informatics and Geosciences, University of Trieste, Trieste, Italy. ¹²iBioTUM – Tissue, Institute of Pathology, School of Medicine, TUM, Munich, Germany. ¹³Institute of Pathology, Technical University of Munich, Munich, Germany. ¹⁴Department of Nephrology, School of Medicine, Technical University Munich, Munich, Germany. ¹⁵Department of Internal Medicine III (Haematology/Medical Oncology), Technical University of Munich Hospital Rechts der Isar, Munich, Germany. ¹⁶Department of General, Visceral and Transplantation Surgery, University Hospital, Ludwig-Maximilians-Universität (LMU) Munich, Munich, Germany. ¹⁷Department of Surgery, TUM University Hospital, rechts der Isar, School of Medicine and Health, Technical University Munich, Munich, Germany. ¹⁸Signalling Research Centres BIOSS and CIBSS, University of Freiburg, Freiburg, Germany. ¹⁹German Cancer Consortium (DKTK) Heidelberg, Germany, Partner Site Freiburg, Freiburg, Germany. ²⁰These authors jointly supervised this work: Michael Quante, Trevor A. Graham. ✉e-mail: melissa.barroux@mri.tum.de; trevor.graham@icr.ac.uk



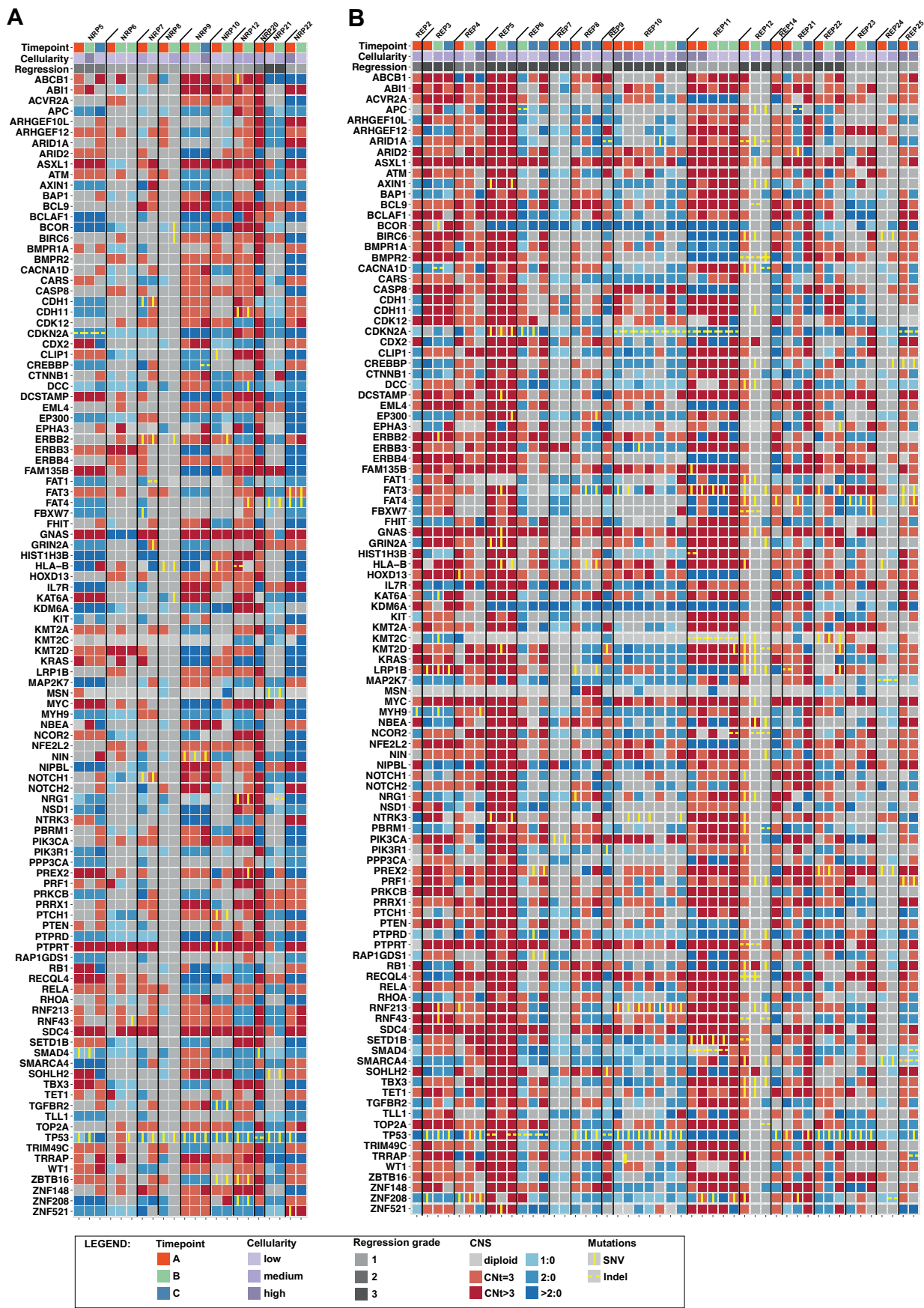
Extended Data Fig. 1 | Clinical data. (a) Principle component analysis of single sample gene set enrichment analysis of cancer hallmark gene sets with color coding of FDG uptake at screening PET-CT. Q1-Q4: lowest to highest quantile of FDG uptake. (b) Proportion of patients with respective Becker regression grades in NRPs (n = 10) and REPs (n = 17) in the cohort for molecular genetic analyses.

(c) Overall survival of NRPs (n = 22) and REPs (n = 45) in the clinical MEMORI cohort. (d) Overall survival of patients with different histopathologic regression grades according to Becker in the clinical MEMORI cohort. (Becker^oI: n = 26; Becker^oII: n = 24; Becker^oIII: n = 17).



Extended Data Fig. 2 | Genetic dynamics in EAC. (a) Tumor cellularity of samples from different timepoints. Tumor cellularity was estimated from whole-exome sequencing data using Sequenza. (b) Violin plots showing the distribution of mutational burden stratified by treatment type (c). Mutations of each sample were classified as clonal or subclonal based on the copy number and cellularity adjusted cancer cell fraction. P values in panels A–C are calculated by the two-sided Wilcoxon test. (d) Selected phylogenetic trees with clade length indicating the number of shared mutations between samples from the

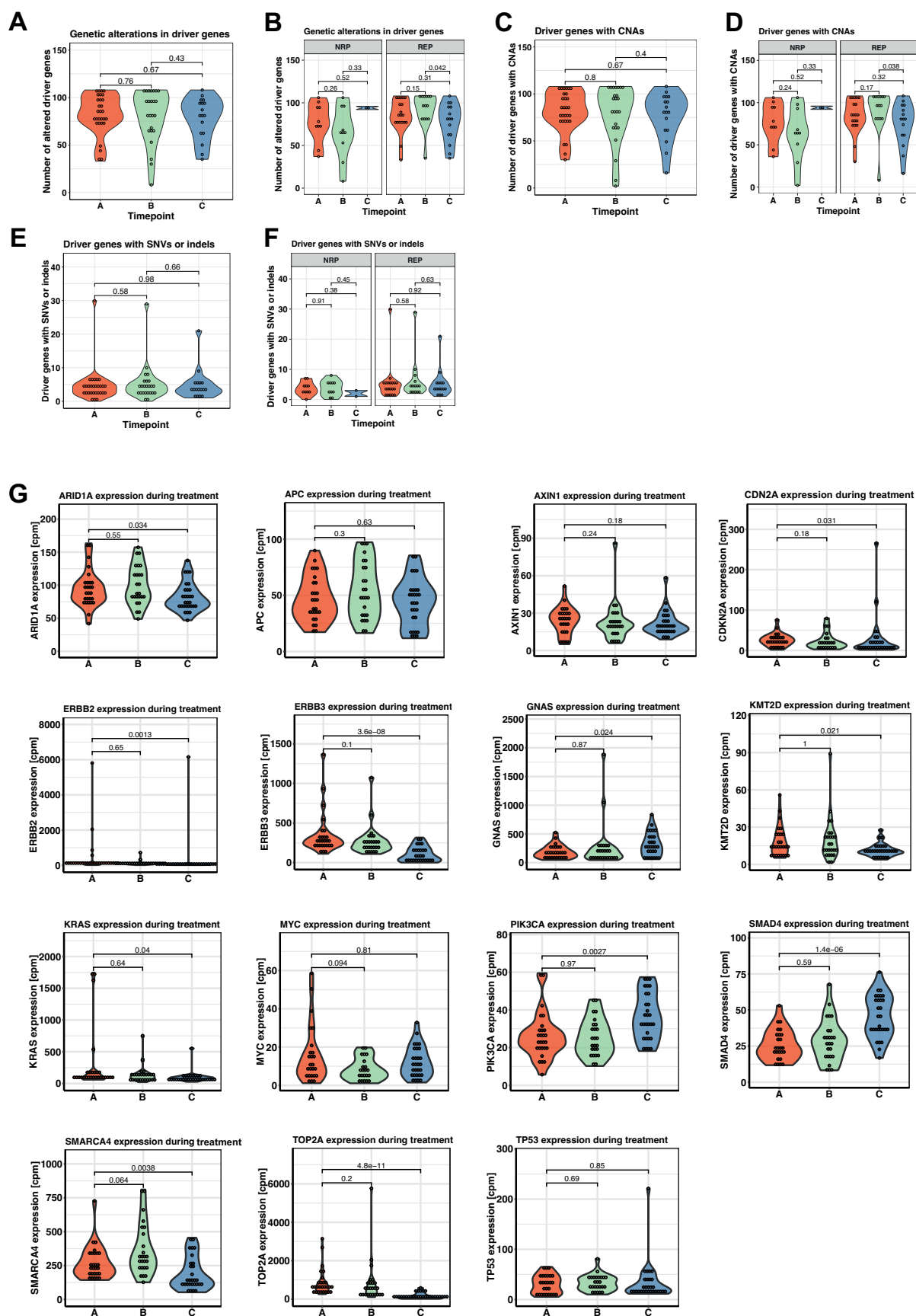
same patient. Timepoint of samples are annotated at the tip of the clades with the letters A–C. Numbers at the nodes indicate bootstrap values. EAC drivers harboring mutations (without brackets) or indels (in squared brackets) and number of neoantigenic SNVs are annotated on the clades of the trees. REP: Responder, NRP: NonResponder, HI: homoplasmy index, NeoSNVs: Neoantigenic single-nucleotide variant. (e) Plot shows COSMIC signature weights of individual samples from NRP (left) and REP (right).



Extended Data Fig. 3 | See next page for caption.

Extended Data Fig. 3 | Genetic alterations in 108 EAC driver genes in NonResponder and Responder. Plot shows genetic alterations, including copy number alterations, SNVs and indels for 108 putative cancer driver genes identified by IntOGen© in NonResponder patients (a) and Responder patients (b). Each vertical column represents a sample. Samples from the same patients are grouped together and patient ID is annotated at the top. Information on timepoint, cancer cellularity and the patient’s pathological regression grade

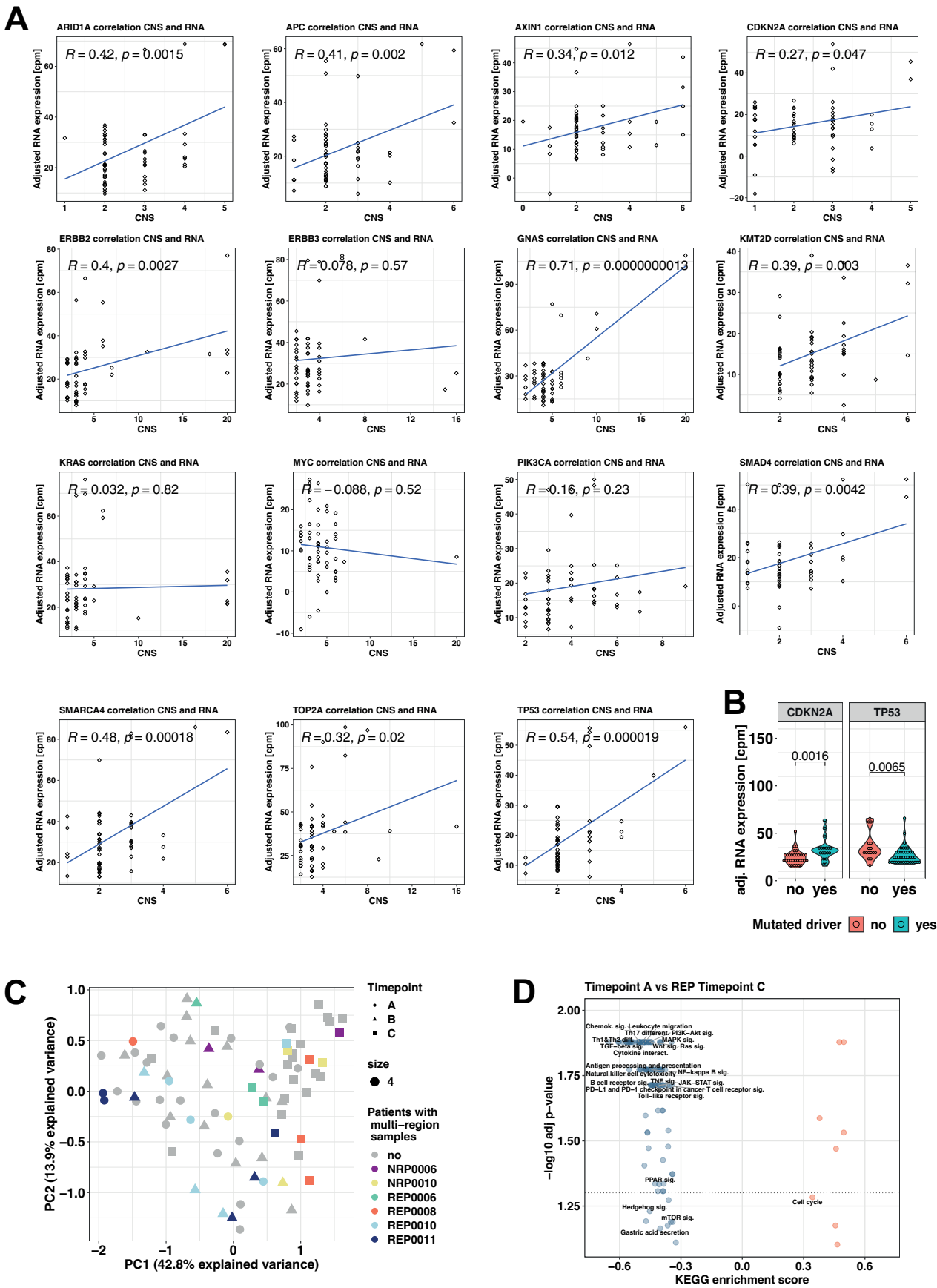
treatment are found in the top three rows. The following rows show information on genetic alterations in EAC driver genes. Cellularity was defined as low (10–40%), medium (41–60%), or high (61–100%). Regression grades were evaluated by a pathologist according to Becker regression classification. CNS: copy number state, CNT: copy numbers, SNV: single-nucleotide variant. REP: Responder, NRP: NonResponder.



Extended Data Fig. 4 | See next page for caption.

Extended Data Fig. 4 | Genetic dynamics and expression of EAC driver genes during treatment. Number of altered (CNA, SNV or indel) genes from 108 EAC drivers in **(a)** the overall cohort, **(b)** NRPs (left) and REPs (right). Number of driver genes with CNAs **(c)** in the overall cohort, **(d)** in NRPs (left) and REPs (right).

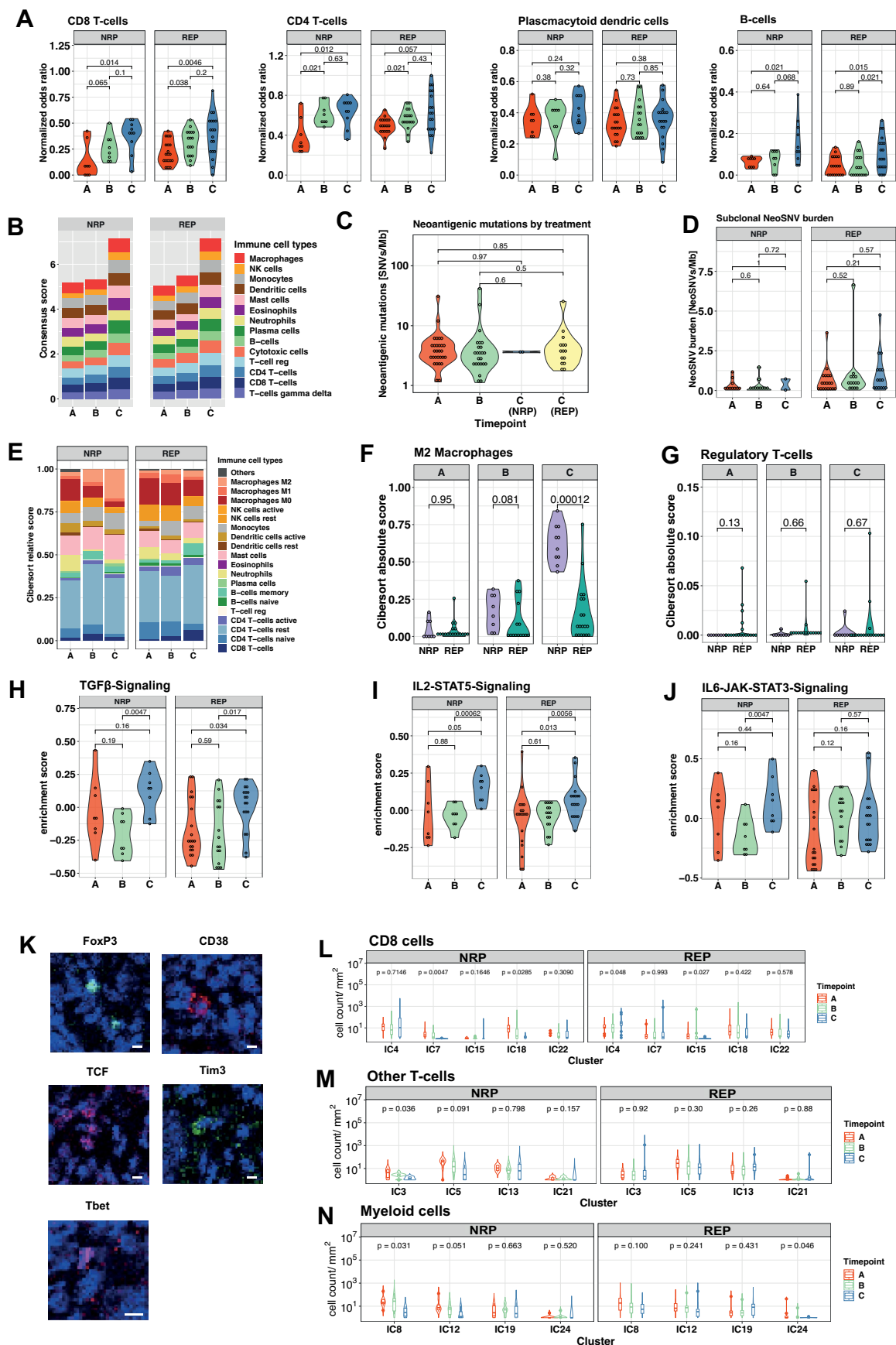
Number of driver genes with SNVs or indels **(e)** in the overall cohort, **(f)** in NRPs (left) and REPs (right). **(g)** Violin plots show expression of 16 high-frequency EAC driver genes during neoadjuvant treatment. P values in all panels are calculated by the two-sided Wilcoxon test. cpm: counts per million.



Extended Data Fig. 5 | See next page for caption.

Extended Data Fig. 5 | Correlations between copy number state/ mutational status and gene expression in high-frequency EAC driver genes. (a) Plot shows correlations between copy number states and tumor cellularity adjusted RNA expression in 15 high-frequency EAC driver genes. RNA expression was adjusted for tumor cellularity estimated by GI pathologist. Correlations were calculated using two-tailed Pearson correlation. CNS: copy number state. (b) Violin plots showing cellularity adjusted RNA expressions of *CDKN2A*/ *TP53*

in *CDKN2A*/ *TP53* mutated and non-mutated samples. P values are calculated by the two-sided Wilcoxon test. (c) Principle component analysis of single sample gene set enrichment analysis of cancer hallmark gene sets. Patients with multi-region samples are highlighted with different colors. PC: Principle component (d) Enrichment analyses in KEGG pathways during chemotherapy (all samples at Timepoint A (n = 27) versus REPs at Timepoint C (n = 19)). Dotted line indicates significance level of $p_{adj} < 0.05$ (FDR-adjusted P values).

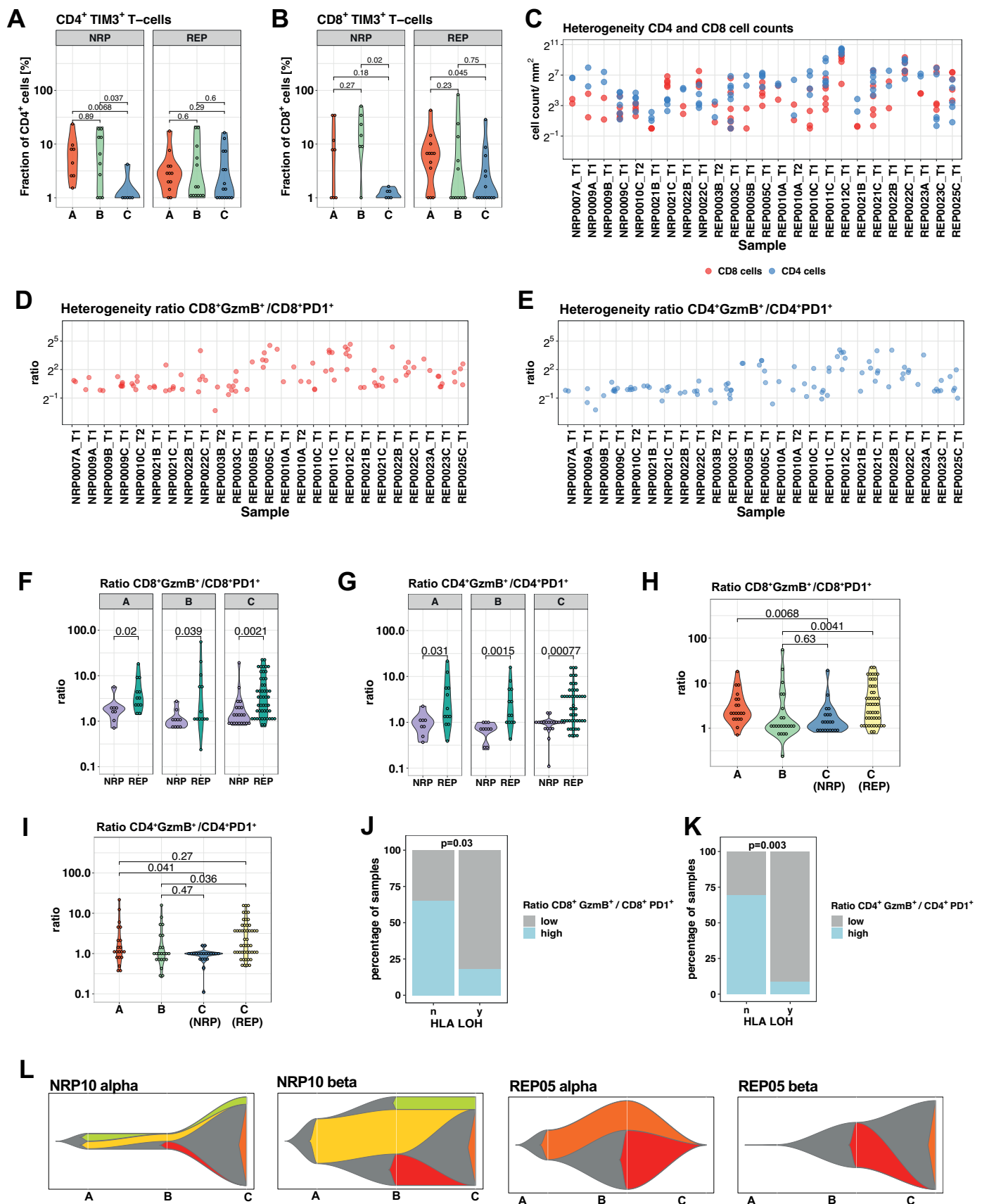


Extended Data Fig. 6 | See next page for caption.

Extended Data Fig. 6 | Immune cell dynamics in EAC during treatment.

(a) Plots show normalized odds ratios for different immune cell types deconvoluted from RNA expression data using Syllolist. (b) Plot shows immune cell scores for different immune cell types deconvoluted from RNA expression data using Consensus^{TME}. Samples from NRP: n = 8 at timepoint A, n = 8 at timepoint B, n = 10 at timepoint C; Samples from REP: n = 19 at timepoint A, n = 16 at timepoint B, n = 19 at timepoint C. Violins showing the (c) neoantigenic mutational burden stratified by treatment regime and (d) the subclonal neoantigenic SNVs in NRPs (left) and REPs (right). (e) Plot shows immune cell proportion based on CIBERSORT analysis in REP and NRP during neoadjuvant treatment. Samples from NRP: n = 8 at timepoint A, n = 8 at timepoint B, n = 10 at timepoint C; Samples from REP: n = 19 at timepoint A, n = 16 at timepoint B, n = 19 at timepoint C. (f) Plots show CIBERSORT scores for M2-macrophages (p-Val at

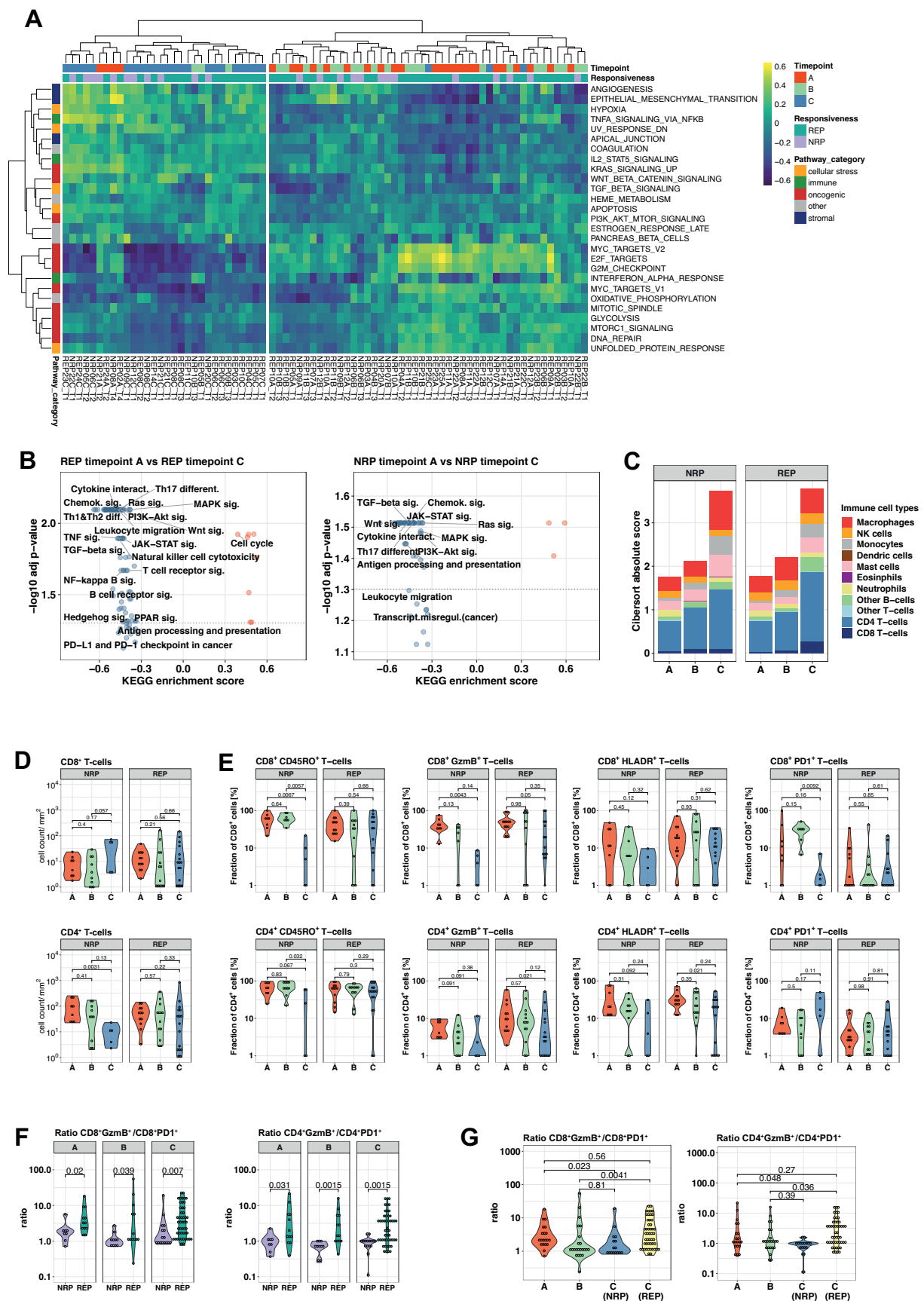
Timepoint C = 0.0001) and (g) regulatory T cells during treatment deconvoluted from RNA expression. (h–j) Enrichment scores for Hallmark of cancer pathways related to immune suppression in NRPs (left) and REPs (right) during treatment. (k) Exemplary visualization of indicated marker expression and DNA (blue) from IMC data. Scale bar: 5µm (l) Dynamics of immune clusters (ICs) with CD8 cells, (m) ICs with other T cells and (n) myeloid cells during treatment are shown by box plots. Box plots show the median, two hinges representing the first and third quartiles and two whiskers showing the minimum and maximum. P values in panels l–n are calculated by the two-sided Kruskal-Wallis test. ROIs from NRPs (n = 8 at timepoint A, n = 10 at timepoint B, n = 6 at timepoint C). ROIs from REPs (n = 12 at timepoint A, n = 13 at timepoint B, n = 16 at timepoint C). P values in all other panels are calculated by the two-sided Wilcoxon test, unless stated otherwise.



Extended Data Fig. 7 | See next page for caption.

Extended Data Fig. 7 | CD4 and CD8 cell dynamics. Fractions of TIM-3-expressing CD4 cells (**a**) and CD8 cells (**b**) in NRPs and REPs during treatment. P values in panels are calculated by the two-sided Wilcoxon test. (**c**) Plot shows heterogeneity of CD4 and CD8 cell counts from IMC analyses in samples where multiple region of interests (ROIs) were analyzed. Dots represent CD4 (blue) or CD8 cell count (red) in individual ROIs. (**d, e**) Heterogeneity of ratio between activated and exhausted CD8 cells (**d**) and CD4 cells (**e**) in samples with multi-region ROIs. Ratio of activated and exhausted CD8 cells (**f**) and CD4 cells (**g**) during treatment including both single and multi-region IMC datasets. Ratio of

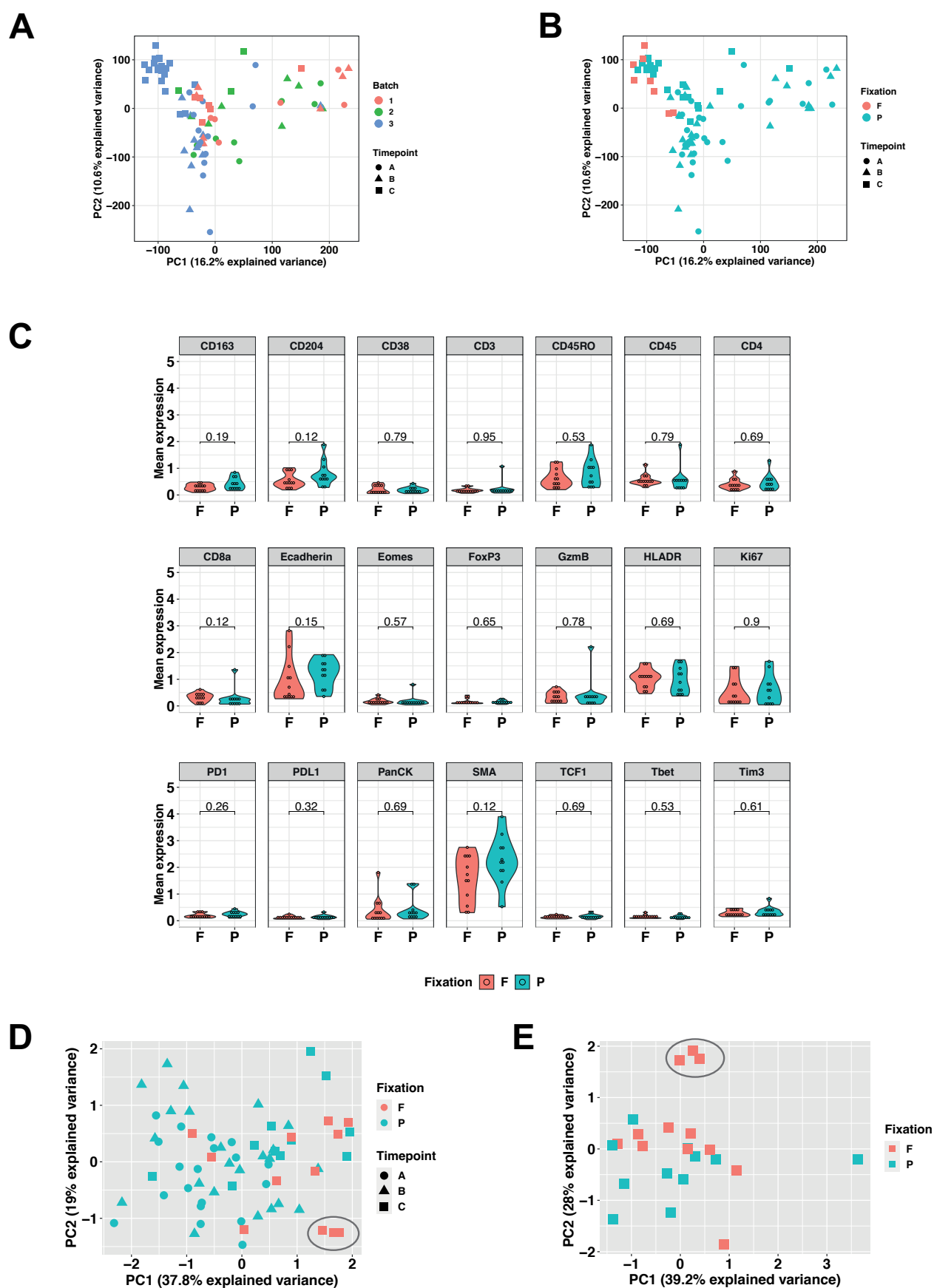
activated and exhausted CD8 cells (**h**) and CD4 cells (**i**) stratified by treatment type. Proportion of high and low CD8 (**j**) and CD4 (**k**) activation status in immune escaped via HLA-LOH (n = 10) and non-escaped (n = 23) samples with matching IMC data. P value is calculated by the two-sided chi-square test. (**l**) Fishplots show the number of 4-fold expanded TCRs between any two timepoints for NRP10 (left panels) and REPO5 (right panels). The colors correspond to the combination of timepoints the TCR expansion occur in. P values in all panels are calculated by the two-sided Wilcoxon test, unless stated otherwise.



Extended Data Fig. 8 | See next page for caption.

Extended Data Fig. 8 | Reanalyzes of immune related results excluding post-treatment samples from patients with complete remission. (a) Hierarchical clustering with heatmap showing the significantly differentially expressed pathways between the two clusters (right cluster is predominantly samples from timepoint A/B and left cluster is predominantly timepoint C). Sample IDs and timepoints are annotated at the bottom of the heatmap. (b) Enrichment in KEGG pathways in Responders between Timepoint A and C (left) and in NonResponder between Timepoint A and C (right). Dotted lines indicate significance level of $p_{\text{adj}} < 0.05$. FDR-adjusted P values. Samples from NonResponder: $n = 8$ at timepoint A, $n = 8$ at timepoint B, $n = 8$ at timepoint C; Samples from Responder: $n = 19$ at timepoint A, $n = 16$ at timepoint B, $n = 18$ at timepoint C. (c) Plot shows immune cell composition based on CIBERSORT analysis in Responders and

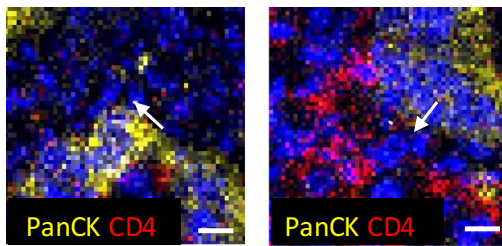
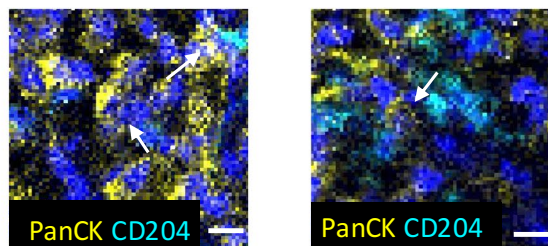
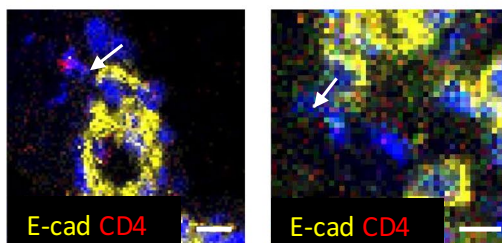
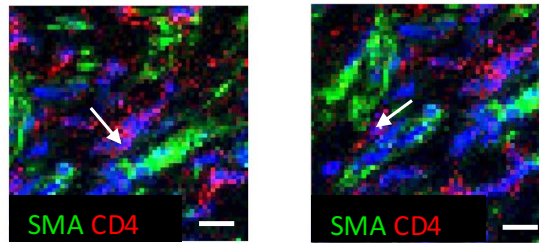
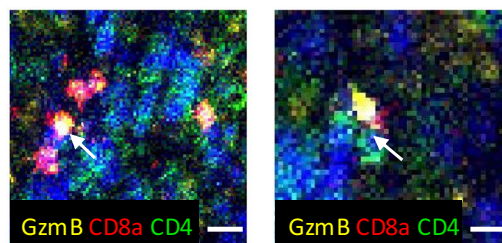
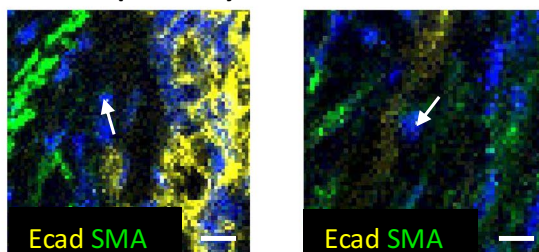
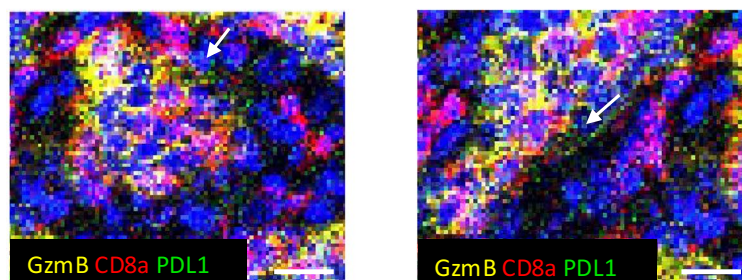
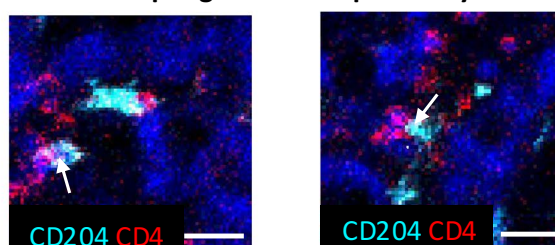
NonResponders during neoadjuvant treatment. Samples from NonResponder: $n = 8$ at timepoint A, $n = 8$ at timepoint B, $n = 8$ at timepoint C; Samples from Responder: $n = 19$ at timepoint A, $n = 16$ at timepoint B, $n = 18$ at timepoint C. (d) Absolute CD4 and CD8 cell counts per mm^2 during treatment. (e) T cell phenotypes in EAC patients during treatment were analyzed for markers of T cell activation and exhaustion. Fractions of CD8 cells (top row) and CD4 cells (bottom row) were compared among patient groups and visualized by violin plots. (f) Ratio of activated and exhausted CD8 cells (left) and CD4 cells (right) during treatment including both single and multi-region IMC datasets. (g) Ratio of activated and exhausted CD8 cells (left) and CD4 cells (right) stratified by treatment type. P values in all panels are calculated by the two-sided Wilcoxon test, unless other stated.



Extended Data Fig. 9 | See next page for caption.

Extended Data Fig. 9 | Unsupervised analyses in PAXgene fixed and formalin-fixed samples. Principle component analysis of RNA-expression data (**a**) in samples of different sequencing batches and (**b**) samples with different fixation methods. F: formalin-fixed samples, P: PAXgene fixed samples. (**c**) Mean expression of included IMC markers in PAXgene fixed samples and formalin-fixed samples samples from Timepoint C. P values in panels are calculated by the two-sided Wilcoxon test. F: formalin-fixed samples, P: PAXgene fixed samples.

(**d**) Principle component analysis of expression-based analysis of included IMC markers including ROIs from all samples. PC: principal component. (**e**) Principle component analysis of expression-based analysis of included IMC markers including ROIs from Timepoint C. PC: principal component. Three samples clustering slightly apart (circled in the PCA) were ROIs from the same patient (REP23).

C1: marginal tumour cells**C4: tumour cells, in direct proximity to macrophages****C6: marginal tumour cells****C11: CD4 and SMA cells in direct proximity****C14: CD4 and CD8 cells in direct proximity****C18: tumour cells and smooth muscle cells in direct proximity****C23: Immune escaped tumour cells, located in proximity to CD8 cells****C24: macrophages in direct proximity to CD4 cells**

Extended Data Fig. 10 | Exemplary staining of cells from ambiguous clusters. Plot shows exemplary stainings of cells from clusters C1, C4, C6, C11, C14, C18, C23 and C24 (white arrow) with respective marker expression. After manual

revision of those clusters, cell types could be attributed. IMC images for unclear clusters were taken from a minimum of 20 cells across different samples. Scale bars: 10 μ m.

Reporting Summary

Nature Portfolio wishes to improve the reproducibility of the work that we publish. This form provides structure for consistency and transparency in reporting. For further information on Nature Portfolio policies, see our [Editorial Policies](#) and the [Editorial Policy Checklist](#).

Statistics

For all statistical analyses, confirm that the following items are present in the figure legend, table legend, main text, or Methods section.

n/a	Confirmed
<input type="checkbox"/>	<input checked="" type="checkbox"/> The exact sample size (<i>n</i>) for each experimental group/condition, given as a discrete number and unit of measurement
<input type="checkbox"/>	<input checked="" type="checkbox"/> A statement on whether measurements were taken from distinct samples or whether the same sample was measured repeatedly
<input type="checkbox"/>	<input checked="" type="checkbox"/> The statistical test(s) used AND whether they are one- or two-sided <i>Only common tests should be described solely by name; describe more complex techniques in the Methods section.</i>
<input type="checkbox"/>	<input checked="" type="checkbox"/> A description of all covariates tested
<input type="checkbox"/>	<input checked="" type="checkbox"/> A description of any assumptions or corrections, such as tests of normality and adjustment for multiple comparisons
<input type="checkbox"/>	<input checked="" type="checkbox"/> A full description of the statistical parameters including central tendency (e.g. means) or other basic estimates (e.g. regression coefficient) AND variation (e.g. standard deviation) or associated estimates of uncertainty (e.g. confidence intervals)
<input type="checkbox"/>	<input checked="" type="checkbox"/> For null hypothesis testing, the test statistic (e.g. <i>F</i> , <i>t</i> , <i>r</i>) with confidence intervals, effect sizes, degrees of freedom and <i>P</i> value noted <i>Give P values as exact values whenever suitable.</i>
<input type="checkbox"/>	<input checked="" type="checkbox"/> For Bayesian analysis, information on the choice of priors and Markov chain Monte Carlo settings
<input type="checkbox"/>	<input checked="" type="checkbox"/> For hierarchical and complex designs, identification of the appropriate level for tests and full reporting of outcomes
<input type="checkbox"/>	<input checked="" type="checkbox"/> Estimates of effect sizes (e.g. Cohen's <i>d</i> , Pearson's <i>r</i>), indicating how they were calculated

Our web collection on [statistics for biologists](#) contains articles on many of the points above.

Software and code

Policy information about [availability of computer code](#)

Data collection	No software was used for data collection.
Data analysis	Skewer v0.2.2 BWA-MEM algorithm v0.7.17 Qualimap v2.2.1 Sequenza-utils v3.0.0 Sequenza R package v2.1.2 Mutect2 v4.1.2.0 ANNOVAR v2018-04-16 bam-readcount MOBSTER v1.0.0 phangorn package v2.11.1 deconstructSigs v 1.8.0 MuTect v1.16 Strelka2 v2.9.9 polysolver v1 neoPredPipe v1 Picard v.2.5.0 DESeq2 v.1.40.2 edgeR v 3.42.4 GSVA v1.48.3

ClusterProfiler 4.8.2
 ConsensusTME v0.0.1.9000
 CyTOF software v7.0
 Ilastik v1.3.3112 and CellProfiler v4.1.3
 histoCAT v1.76
 OMIQ

For manuscripts utilizing custom algorithms or software that are central to the research but not yet described in published literature, software must be made available to editors and reviewers. We strongly encourage code deposition in a community repository (e.g. GitHub). See the Nature Portfolio [guidelines for submitting code & software](#) for further information.

Data

Policy information about [availability of data](#)

All manuscripts must include a [data availability statement](#). This statement should provide the following information, where applicable:

- Accession codes, unique identifiers, or web links for publicly available datasets
- A description of any restrictions on data availability
- For clinical datasets or third party data, please ensure that the statement adheres to our [policy](#)

Gene expression data, somatic mutation calls (MuTect2 and Annovar), copy-number calls (Sequenza), neoantigen calls (Nepred pipeline) and called TCRs are available on Mendeley (doi: 10.17632/brsxy4746.1)80. MCD files and cell segmentation files (IMC analyses) have been deposited at Zenodo (<https://doi.org/10.5281/zenodo.12800339>). Sequencing data have been deposited at the European Genome-phenome Archive, under the accession numbers (EGAS50000000240; EGAS50000000242). Access to these bam files is controlled and subject to application via the EGA platform. The accession of bam files is limited to research purposes and regulated with a data use agreement. The timeframe for response to requests is expected within 10 working days. Further information about the European Genome-phenome Archive can be found at <https://ega-archive.org>. Source data for all figures have been provided as Source Data files.

Research involving human participants, their data, or biological material

Policy information about studies with [human participants or human data](#). See also policy information about [sex, gender \(identity/presentation\), and sexual orientation](#) and [race, ethnicity and racism](#).

Reporting on sex and gender

The research findings do not apply to only one sex or gender. We report information on patients' sex in figure 1 and supplemental table 1. Sex and gender were not considered in the study design. In this study samples from 25 male and 2 female patients have been analyzed. Information on gender has not been collected and is therefore not reported. Consent has been obtained for sharing individual-level data. Post hoc sex- and gender-based analysis have not been performed as the study design is insufficient for sex- and gender-based analysis due to low sample size.

Reporting on race, ethnicity, or other socially relevant groupings

Information on race, ethnicity or other socially relevant groupings has not been collected and is therefore not reported.

Population characteristics

Population characteristics such as sex, age and ECOG performance status have been reported in supplemental table 1.

Recruitment

EAC specimens were obtained from the prospective clinical MEMORI trial. All patients with locally advanced EAC who attended Technical University Munich and University Hospital Ludwig-Maximilians-Universitaet were asked to participate in the MEMORI trial. Patients who gave informed consent were screened for the MEMORI trial. Patients with locally advanced EAC and intense FDG tracer uptake of the tumour at baseline FDG-PET-CT ([18F] - FDG uptake in the tumor at baseline > 1.35 x liver SUV + 2x standard deviation of the liver SUV) and thus suitable for monitoring and early response prediction by FDG - PET were eligible for MEMORI trial. The inclusion criteria of intense FDG tracer uptake in the treatment naive tumour, might lead to a selection bias of patients with a higher tumour metabolism. Among included patients, FDG uptake intensity was not associated with global transcriptomic differences (Extended Data fig 1A), suggesting no major stratification in biologically different subgroups based on initial PET signal intensity. We can not exclude any self-selection biases of the MEMORI cohort, which occurs in every clinical trial when the decision to participate in a study is left entirely up to individuals. We do not expect that self-selection bias affects the translational results of our study.

Ethics oversight

The MEMORI trial protocol was approved by the local ethics committee at Technical University Munich. All patients gave written informed consent for collection and molecular analysis of their sample material and the inclusion of the information listed in the manuscript within the MEMORI trial protocol. The study protocol is available on request.

Note that full information on the approval of the study protocol must also be provided in the manuscript.

Field-specific reporting

Please select the one below that is the best fit for your research. If you are not sure, read the appropriate sections before making your selection.

☒ Life sciences ☐ Behavioural & social sciences ☐ Ecological, evolutionary & environmental sciences

For a reference copy of the document with all sections, see nature.com/documents/nr-reporting-summary-flat.pdf

Life sciences study design

All studies must disclose on these points even when the disclosure is negative.

Sample size	No statistical methods were used to pre-determine sample sizes but our sample sizes are similar to those reported in previous publications: Findlay, J. M. et al. Differential clonal evolution in oesophageal cancers in response to neo-adjuvant chemotherapy. Nature communications 7, 11111, doi:papers2://publication/doi/10.1038/ncomms11111 (2016). Murugaesu, N. et al. Tracking the genomic evolution of esophageal adenocarcinoma through neoadjuvant chemotherapy. Cancer discovery 5, 821-831, doi:papers2://publication/doi/10.1158/2159-8290.CD-15-0412 (2015). Verschoor, Y. L. et al. Neoadjuvant atezolizumab plus chemotherapy in gastric and gastroesophageal junction adenocarcinoma: the phase 2 PANDA trial. Nat Med 30, 519-530, doi:10.1038/s41591-023-02758-x (2024).
Data exclusions	Various data exclusions were performed on an analysis-by-analysis basis (usually due to available sample numbers with required tumour tissue or multi-omics quality). These are specified in the manuscript at the point that each analysis is described.
Replication	Specific replication on individual samples was not possible due to insufficient material.
Randomization	Randomization was not relevant to this study. The explicit analysis clinical-pathological of covariates, such as treatment responsiveness, is reported in the manuscript. Our study was an observational cohort study so randomization was not possible. No differential outcomes were examined so randomization was not needed.
Blinding	Data collection and analysis were not performed blind to the clinical subgroups of the experiments.

Reporting for specific materials, systems and methods

We require information from authors about some types of materials, experimental systems and methods used in many studies. Here, indicate whether each material, system or method listed is relevant to your study. If you are not sure if a list item applies to your research, read the appropriate section before selecting a response.

Materials & experimental systems

n/a	Involved in the study
<input type="checkbox"/>	<input checked="" type="checkbox"/> Antibodies
<input checked="" type="checkbox"/>	<input type="checkbox"/> Eukaryotic cell lines
<input checked="" type="checkbox"/>	<input type="checkbox"/> Palaeontology and archaeology
<input checked="" type="checkbox"/>	<input type="checkbox"/> Animals and other organisms
<input type="checkbox"/>	<input checked="" type="checkbox"/> Clinical data
<input checked="" type="checkbox"/>	<input type="checkbox"/> Dual use research of concern
<input checked="" type="checkbox"/>	<input type="checkbox"/> Plants

Methods

n/a	Involved in the study
<input checked="" type="checkbox"/>	<input type="checkbox"/> ChIP-seq
<input checked="" type="checkbox"/>	<input type="checkbox"/> Flow cytometry
<input checked="" type="checkbox"/>	<input type="checkbox"/> MRI-based neuroimaging

Antibodies

Antibodies used	<p>IMC antibodies used for IMC analysis</p> <p>Target, clone, company, cat#, dilution</p> <p>HLA-DR, TAL-1B5, Abcam, ab176408, 1:400</p> <p>SMA, 1A4, Standard Biotoools, 3141017D, 1:1600</p> <p>Ki-67, B56, BD, 556003, 1:200</p> <p>CD163, EDhu-1, Standard Biotoools, 3147021D, 1:1600</p> <p>Pan-keratin, C-11, Standard Biotoools, 3148020D, 1:200</p> <p>PD-L1, E1L3N, CST, 13684BF, 1:90</p> <p>TCF-1, C63D9, CST, 2203BF, 1:100</p> <p>Tim-3, D5D5R, Standard Biotoools, 3154024D, 1:1600</p> <p>FoxP3, 236A/E7, Thermo Fisher, 14-4777-82, 1:200</p> <p>CD4, EPR6855, Abcam, ab181724, 1:400</p> <p>E-cadherin, 24 E 10, Standard Biotoools, 3031901, 1:200</p> <p>T-bet, 4B10, BioLegend, 644802, 1:100</p> <p>CD8a, C8/144B, BioLegend, 372902, 1:1600</p> <p>Eomes, WD1928, Thermo Fisher, 14-4877-82, 1:200</p> <p>PD-1, D4W2J, CST, 86163BF, 1:200</p> <p>CD204, J5HTR3, Thermo Fisher, 14-9054-82, 1:400</p> <p>GranzymeB, EPR20129-217, Standard Biotoools, 3167021D, 1:1600</p> <p>CD38, EPR4106, Abcam, ab176886, 1:100</p> <p>CD45RO, UCHL1, BioLegend, B265383, 1:800</p> <p>DNA1, NA, Standard Biotoools, 201192B, 1:2000</p> <p>DNA2, NA, Standard Biotoools, 201192B, 1:2000</p>
-----------------	--

Validation

Target, Clone, Citation

HLA-DR, TAL-1B5, "Ijsselsteijn M, et al. 2019. Front. Immunol. 10:2534."
 SMA, 1A4, "Schlecht A, et al. 2021. BMC Ophthalmology. 21(1):338."
 Ki-67, B56, "Schwablenland M, Salié H, et al. 2021. Immunity. 54(7):1594-1610"
 CD163, EDhu-1, "Schwablenland M, Salié H, et al. 2021. Immunity. 54(7):1594-1610"
 Pan-keratin C-11, "Ijsselsteijn M, et al. 2019. Front. Immunol. 10:2534."
 PD-L1, E1L3N, "Ijsselsteijn M, et al. 2019. Front. Immunol. 10:2534."
 TCF-1, C63D9, "Schwablenland M, Salié H, et al. 2021. Immunity. 54(7):1594-1610"
 Tim-3, D5D5R, "Ijsselsteijn M, et al. 2019. Front. Immunol. 10:2534."
 FoxP3, 236A/E7, "Schwablenland M, Salié H, et al. 2021. Immunity. 54(7):1594-1610"
 CD4, EPR6855, "Ijsselsteijn M, et al. 2019. Front. Immunol. 10:2534."
 E-cadherin, 24 E 10, "Schlecht A, et al. 2021. BMC Ophthalmology. 21(1):338."
 T-bet, 4B10, "Ijsselsteijn M, et al. 2019. Front. Immunol. 10:2534."
 CD8a, C8/144B, "Sade-Feldman M, et al. 2018. Cell. 175:998"
 Eomes, WD1928, "Schwablenland M, Salié H, et al. 2021. Immunity. 54(7):1594-1610"
 PD-1, D4W2J, "Ijsselsteijn M, et al. 2019. Front. Immunol. 10:2534."
 CD204, J5HTR3, "Ijsselsteijn M, et al. 2019. Front. Immunol. 10:2534."
 GranzymeB, EPR20129-217, "Schwablenland M, Salié H, et al. 2021. Immunity. 54(7):1594-1610"
 CD38, EPR4106, "Ijsselsteijn M, et al. 2019. Front. Immunol. 10:2534."
 CD45RO, UCHL1, "Ijsselsteijn M, et al. 2019. Front. Immunol. 10:2534."
 DNA1, NA, M, Salié H, et al. 2021. Immunity. 54(7):1594-1610"
 DNA2, NA, "Schwablenland M, Salié H, et al. 2021. Immunity. 54(7):1594-1610"

Clinical data

Policy information about [clinical studies](#)

All manuscripts should comply with the ICMJE [guidelines for publication of clinical research](#) and a completed [CONSORT checklist](#) must be included with all submissions.

Clinical trial registration

Study protocol

Data collection

Outcomes

Plants

Seed stocks

Novel plant genotypes

Authentication